Energy exchange in a dense urban environment Part II: impact of spatial heterogeneity of the surface

Article

Published Version

Open Access

It is advisable to refer to the publisher's version if you intend to cite from the work.

www.reading.ac.uk/centaur

CentAUR

Central Archive at the University of Reading

Reading's research outputs online

CrossMark

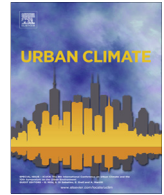# Energy exchange in a dense urban environment – Part II: Impact of spatial heterogeneity of the surface

Simone Kotthaus *, C.S.B. Grimmond

Earth and Environmental Dynamics, Department of Geography, King's College London, The Strand, London WC2R 2LS, UK
Department of Meteorology, University of Reading, Earley Gate, PO Box 243, Reading RG6 6BB, UK

ARTICLE INFO

ABSTRACT

The centre of cities, characterised by spatial and temporal complexity, are challenging environments for micrometeorological research. This paper considers the impact of sensor location and heterogeneity of the urban surface on flux observations in the dense city centre of London, UK. Data gathered at two sites in close vicinity, but with different measurement heights, were analysed to investigate the influence of source area characteristics on long-term radiation and turbulent heat fluxes. Combining consideration of diffuse radiation and effects of specular reflections, the non-Lambertian urban surface is found to impact the measurements of surface albedo. Comparisons of observations from the two sites reveal that turbulent heat fluxes are similar under some flow conditions. However, they mostly observe processes at different scales due to their differing measurement heights, highlighting the critical impact of siting sensors in urban areas. A detailed source area analysis is presented to investigate the surface controls influencing the energy exchanges at the different scales.

© 2013 Elsevier B.V. All rights reserved.

1. Introduction

Surface characteristics, such as the arrangement of roughness elements, the locations of heat and moisture sources, or the texture of materials, all play a role in the formation of climate conditions in

---

* Corresponding author at: Department of Meteorology, University of Reading, Earley Gate, PO Box 243, Reading RG6 6BB, UK. Tel.: +44 118 378 5419.

E-mail address: s.kotthaus@reading.ac.uk (S. Kotthaus).

the lowest part of the atmosphere. Urban areas often have a particularly complex mix of surface materials, with buildings and roads (made of e.g. concrete or asphalt), right next to vegetation (e.g. street trees, gardens or parks) or water bodies (e.g. rivers or lakes). This combination of surface materials and their spatial arrangement are instrumental in generating distinct urban climates. The manipulation of these so called 'blue/green/grey' surfaces is core to many sustainable urban planning strategies aimed at mitigating negative urban climatic effects. The diversity of surface characteristics creates challenges for boundary layer and urban meteorology research and applications. This spatial variability has implications for all studies of the urban climate, independent of measurement technique or modelling approach. Scale and representativeness become central issues to consider when results obtained with different techniques are combined (Schmid, 1997).

To date, the spatial variability of urban eddy covariance energy flux measurements have been addressed in three ways. First, intra-urban variations have been evaluated through simultaneous observations at multiple sites within a city (e.g. Basel, Christen and Vogt, 2004; Łódź, Offerle et al., 2006; Melbourne, Coutts et al., 2007; Essen, Weber and Kordowski, 2010; Helsinki, Nordbo et al., 2012), in some cases with a rural reference site. Second, variations of turbulent sensible heat fluxes within one land use unit have been observed for short periods (e.g. multiple sites in a suburban area of Vancouver at the local-scale, Schmid et al., 1991; in a densely built up residential area of Tokyo within the roughness sublayer, Kanda et al., 2006). Third, vertical flux variations have been investigated (e.g. Rotach, 1995; Grimmond et al., 2004), allowing consideration of where the blending height or top of the roughness sublayer may be located.

Given the patchiness of the urban surface and its complex roughness characteristics it is often challenging to undertake EC observations in urban areas that are representative of a local-scale land use (e.g. Schmid et al., 1991; Vesala et al., 2008a; Feigenwinter et al., 2012). However, the need to better understand energy exchange processes in these environments is leading to an increase in the number of EC sites being operated – even in dense city centres such as in this study. The objective of this study is to investigate how flux observations can be used to study energy exchanges in a dense urban city centre. Here two nearby sites with different measurement heights in London (UK) are analysed with respect to the impact of site location and heterogeneity of the urban surface on flux observations. Evaluation is made as to whether simple source area modelling can aid interpretation of the results and the aspects most crucial to improve understanding. Details of the measurements (e.g. data collection, processing methods) and their temporal variability are presented in a companion paper (Kotthaus and Grimmond, 2013). First the methodology for footprint calculations is presented (Section 2). Second, the surface influence on short-wave radiative fluxes is analysed (Section 3). Third, the spatial variations of the observed turbulent fluxes are interpreted with respect to their source areas and a comparison between two nearby sites is presented (Section 4). Implications of these findings for turbulent flux source area modelling in urban areas and the critical aspect of siting are discussed (Section 5). Conclusions of this study (Section 6) outline both the challenges of energy flux observations in dense urban settings and the new interpretations obtained.

2. Methods

Net all-wave radiation Q^* and the turbulent fluxes of sensible heat Q_H and latent heat Q_E are important components of the surface energy exchange in urban areas (Oke, 1987). For this study, all three were obtained by *in-situ* observations. The companion paper Kotthaus and Grimmond (2013) provides details on these and other surface energy balance components.

2.1. Measurement site

The study area is located in the 'Central Activities Zone' (CAZ) of London, UK (see Kotthaus and Grimmond, 2013 for further details). At the Strand Campus of King's College London (KCL, 51°30′ N, 0°7′ W), two measurement towers, referred to as *KSS* and *KSK*, were located approximately 60 m apart (Fig. 1).
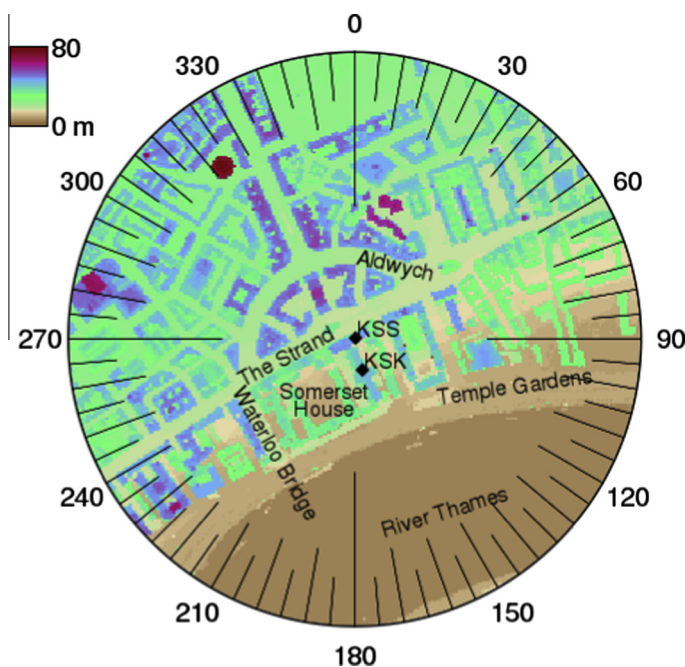
Fig. 1. Digital elevation model of ground and buildings (Lindberg and Grimmond, 2010) for a 500 m radius around KCL Strand (centred on KSS site) in metres above sea level at 4 m spatial resolution. Radial coordinates according to BNG (British National Grid) north. Site locations and relevant places are labelled.

Urban sites can be characterised using a number of techniques including image based classification (e.g. LCZ, Local Climate Zone, Stewart and Oke, 2012) or simple models (e.g. UZE, Urban Zone for Energy partitioning, Loridan and Grimmond, 2012) which provide expectations of the urban heat island intensity and energy flux partitioning. Around KCL, the LCZ is 'compact midrise' and the UZE is 'high density'. More detailed descriptions of surface cover, derived from source area modelling are presented in Section 4.2. Sensors were mounted on the top of extendable towers (KSK: single tube mast, Clark Masts CSQ T97/HP; KSS: triangular tower, Aluma T45-H), with the towers installed on the top of buildings. At KSS (KSK) the measurement height above ground level (agl) was 49 m (39 m); a ratio of 2.2 (1.9) compared to mean building height z_h. The River Thames, in close vicinity of the sites (Fig. 1), experiences tidal differences of up to 6 m.

KCL Strand is located at a junction (*Aldwych*) of one of the main east–west roads through central London, *The Strand*. Taxis, private cars and buses (including several night bus routes) use this road with high frequency. In addition, vans and lorries deliver goods to businesses, shops, restaurants and hotels in the area. Especially during rush hour, substantial traffic emissions can be expected. To the southwest is a pedestrian courtyard within *Somerset House* (Fig. 1) and another busy road (*Waterloo Bridge*).

2.2. Data collection and processing

The turbulent fluxes of sensible and latent heat were observed using the eddy covariance (EC) method. Net all-wave radiation was measured directly and auxiliary meteorological observations and cloud cover were also observed at KCL Strand. In this paper, data collected between October 2008 and March 2012 are used. While turbulent heat fluxes were calculated based on 30 min intervals, all other data are available with a resolution of 15 min. At KSK, two *Kipp & Zonen* radiometers have been operational (Kotthaus and Grimmond, 2013, their Table 1): a CNR1 (2008–2009) and CNR4 (2010–2012). Based on daily total incoming short-wave radiation, the estimates by the older sensor (CNR1) are

Table 1
Site and source area characteristics at KSK and KSS calculated as averages over all available observations based on the individual turbulent source area estimates. Heights specified in m above ground level (agl).

		KSK	KSS
Height [m agl]	Mean building height z_h	21.0	22.0
	Roughness length z_0	1.7	1.9
	Displacement height z_d	13.8	14.2
	Sensor height z_m	38.8	48.9
	Height of building hosting tower	30.2	35.6
Height [m]	Tower height above roof	8.6	13.3
Turbulent source area [km²]	Including 50% of footprint	0.1	0.2
	Including 90% of footprint	3.0	5.3
Distance X_{max} from site to footprint maximum [m]	Unstable atm. conditions	67	95
	Neutral atm. conditions	101	147
Land cover fraction in source area [%]	Roads	43	43
	Buildings	40	38
	Water	13	14
	Vegetation	4	5

higher by ∼6%. This falls in the range of expected accuracy of ±10% specified by the manufacturer for daily totals. Cloud cover percentage was estimated based on ceilometer backscatter information, aggregated to the same temporal resolution. All recording and data analysis was done in UTC (Universal Time Coordinated). This is local time in the winter and an hour earlier during the summer (daylight savings period). Further information on data collection, availability, and processing is provided by Kotthaus and Grimmond (2013).

2.3. Source area calculations

Micrometeorological measurements characterise surface-atmosphere exchange as a function of the radiative properties, moisture availability, or anthropogenic activities etc. of the surface. With a complex surface the linkage between the measurement and instrumental source area becomes more challenging. Of particular interest in this study is the influence of surface controls in a dense urban setting. Approaches to source area modelling are described as context for the measurement methods used.

2.3.1. Turbulent flux footprint

The turbulent fluxes of latent and sensible heat change in time and space as a function of sensor position (height; e.g. Schmid and Lloyd, 1999), atmospheric conditions (expressed by e.g. wind speed, wind direction, atmospheric stability; e.g. Kljun et al., 2002) and surface characteristics (expressed by e.g. terrain, surface roughness, material composition; e.g. Vesala et al., 2008b).

Observed urban turbulent energy exchanges are commonly stratified by wind direction into sectors related to land cover (e.g. Järvi et al., 2009 compare roads, buildings and vegetation). This practice takes into account two very important aspects of the linkage between the surface and observed turbulent exchange: wind direction and broad variations in surface characteristics. However, it does not provide any insight in the effect of wind speed (e.g. related to mesoscale wind regimes, Lemonsu et al., 2004) or atmospheric stability. The latter is a major control on the extent of the source area (Kljun et al., 2002).

Footprint models of varying complexity have been developed to locate the probable surface area affecting turbulent flux measurements (see review in Vesala et al., 2010). After pioneering work on analytical footprint calculations (e.g. Gash, 1986; Schuepp et al., 1990; Horst and Weil, 1992), a 3D analytical model (scalar Flux Source Area Model, FSAM) was developed to aid interpreting eddy covariance measurements (Schmid 1994, 1997). This has been widely used in a variety of urban studies, e.g. supporting energy balance analysis in Marseille (Grimmond et al., 2004; Lemonsu et al., 2004), carbon dioxide flux observations in Essen (Kordowski and Kuttler, 2010), and a series of turbulent flux measurements in Łódź (Offerle et al., 2006; Pawlak et al., 2011; Fortuniak et al., 2012).

Future computing capacity will make the applicability of Lagrangian stochastic dispersion models that can represent complex flow conditions more feasible. However, such sophisticated models have not yet been used in full for urban studies. A simple parameterisation (Kljun et al., 2004) of the backward trajectory Lagrangian stochastic footprint model of Kljun et al. (2002) has been applied to urban situations (e.g. Mårtensson et al., 2006; Hiller et al., 2011; Park et al., 2011). Hsieh et al.'s (2000) analytical footprint model, a parameterisation from a Lagrangian stochastic approach, aided interpretation of carbon dioxide fluxes in Florence (Gioli et al., 2012). The forward Lagrangian stochastic model of Göckede et al. (2006), based on an analytical method (FSAM), identified the probable source areas for small aperture scintillometers in a dense city centre (Pauscher, 2010).

More sophisticated methods, such as Large Eddy Simulation (LES) or ensemble-averaged closure models (Rannik et al., 2012), tend to be computationally expensive and address restricted stability conditions. Hence, they remain minimally used in city studies. Vesala et al. (2008b) apply the model SCADIS (Sogachev and Lloyd, 2004; Sogachev, 2009) to a Helsinki site but only under neutral conditions for two wind directions, where they find an asymmetry of the source area in the approaching flow.

The relatively simple implementation of analytical footprint models provides clear advantages in computing time and ease of use, so they are often applied to gain a first order estimate of probable location and size of flux source areas (Rannik et al., 2012). Some uncertainty might arise from simplifications (van de Boer et al., 2011) as these models are not capable of formulating the whole complexity of the surface flow. Developed for flat surfaces they are not able to capture the impact of vertical variations of sources and sinks (Vesala et al., 2008a; Salmond et al., 2012). Nonetheless, the information gained from more elaborate models does not (yet) legitimate their complexity and time intensive implementation for large datasets. Thus, analytical models are usually chosen for the interpretation of long-term datasets. Recent examples of their application include the Kormann and Meixner (2001) model to interpret carbon dioxide fluxes (e.g. Vancouver, Christen et al., 2011; Baltimore, Crawford et al., 2011; Beijing, Liu et al., 2012), to improve understanding of turbulent energy transport (e.g. Helsinki, Nordbo et al., 2012; Basel, Salmond et al., 2012) and to match *in-situ* and remote sensing observations (e.g. Cairo, Frey and Parlow, 2012).

The footprint calculated for individual time periods can be composited by time and space to provide, with an appropriate geographical information database, the sensor field of view or footprint climatology. Such an approach has been shown to be beneficial to the interpretation of urban fluxes (e.g. Christen et al., 2011).

In this study, footprint functions for both study sites for each 30 min period were estimated with the Kormann and Meixner (2001) analytical footprint model. However, instead of calculating friction velocity (u^*) according to Eq. (31) in Kormann and Meixner (2001), the measured value of u^* at the respective site (KSK or KSS) was supplied to the footprint model as input, along with wind speed, wind direction, cross wind standard deviation σ_v and Obukhov length L. Roughness length for momentum z_0 and displacement height z_d were estimated using Macdonald et al.'s (1998) method based on the mean building height above ground z_h, plan area fraction λ_p and frontal area index λ_f. All three morphometric parameters were calculated from a digital elevation model (DEM) of ground and buildings at a spatial resolution of 4 m (Lindberg and Grimmond, 2010).

Vegetation covers a small portion of the area around the study sites, thus its effect on surface roughness is assumed to be negligible. The topography of the area slopes from the lowest elevations at the river to highest in the north (Fig. 1). To incorporate these variations, mean ground height z_g as well as z_h, λ_p and λ_f were estimated as a function of wind direction. First, a database of morphometric parameters was created based on a 500 m radius and 1° intervals. These were then averaged based on mean sectors (defined by mean wind direction and cross wind variability σ_v) to derive 'first-guess' estimates of roughness parameters z_0 and z_d for each time period. These were then used in the initial footprint calculation. New morphometric parameters were calculated for each identified source area, leading to new roughness parameters that provided the basis for more precise source area calculations. Finally, morphometric parameters and land cover fractions were obtained from this area for each observation period. In order to facilitate the analysis, these results have then been aggregated into 10° wind sectors. The measurement height z_m was adjusted during this iterative process to account for variations in ground height. This is crucial because the effective height $z' = z_m - z_d$ was used

within the atmospheric stability parameter $\zeta = z'/L$ to classify unstable ($\zeta < -0.1$), near-neutral ($-0.1 \leqslant \zeta < 0.1$), and stable ($0.1 \leqslant \zeta$) conditions.

2.3.2. Radiometer footprint

Key to surface atmosphere exchanges are radiative fluxes. For Lambertian surfaces, the source area is mainly a function of measurement height. However, the complex three-dimensional structure of the urban surface causes shadow patterns and the combination of various materials with different radiative properties brings about spatial variability caused by the sun-surface geometry (Soux et al., 2004). High reflectance materials such as glass and metal are increasingly used in modern architecture, especially for commercial buildings, leading to distinct reflections of short-wave radiation. 'Reflection glare' can cause discomfort, and even danger, to the urban population (e.g. people working in offices, pedestrians or drivers, Iwata et al., 1991). Strong reflections of solar radiation from vertical facets, or even horizontal surfaces, increase short-wave (including UV) but also thermal energy gain to the object receiving the reflected beam (Shih and Huang, 2001).

Measurement of surface albedo is impacted not only by surface materials and their spatial arrangement but also by the atmospheric transmissivity and solar geometry. As atmospheric transmissivity determines the relation between diffuse and direct solar irradiance (Lucht et al., 2000) the total surface albedo includes the reflection of diffuse (white-sky albedo) and direct (black-sky albedo) radiation. While the black-sky albedo can be expressed as a function of the solar elevation angle, the interaction of diffuse radiation with the surface should be independent of solar geometry (Lucht et al., 2000).

The footprints of EC and radiation measurements usually do not agree (Schmid, 1997) as different processes control the respective energy transfer. Concentric circles describe isopleths of the source area of a radiometer (over a Lambertian surface) which do not vary temporarily. Their radii depend on the measurement height above the surface (Schmid, 1997). For non-Lambertian surfaces, this source area model can provide a first approximation of the footprint for the case of diffuse irradiance when variations in directional reflectance of the surface have less impact. Under direct irradiance, however, heterogeneities in surface reflectance can represent great variations in the surface response, thereby inducing a complex pattern of source area weights that can no longer be represented by concentric circles. Here the footprint function should incorporate the bidirectional reflectance distribution function (BRDF) of the surface as well as the sun geometry, which varies both spatially and temporally. In an urban setting, the BRDF needs to combine variations due to surface materials but also the three-dimensional form of buildings, vegetation, roads, and canyons. This is unique for every measurement site and sensor height, and very difficult to portray.

In this study, in order to visualise the impact of the urban surface on reflected short-wave radiation, locations of maximum specular reflection were calculated as a function of solar azimuth angle and distance of maximum reflection of solar irradiance

$$R_s = z_R / \tan \Theta$$

with sun elevation angle Θ and height of the pyranometer above the surface z_R. This formulation of the radius of maximum specular reflection R_s stems from rules of specular reflectance and basic geometry. Given the majority of the pyranometers' field of view (FOV) consisted of roof surfaces, the height above the surface z_R was assigned as an average value defined as the tower height above the roof reduced by 1 m to account for roof height variations and objects (such as elevated windows) close to the towers. Even though this measure assumes a flat surface and does not account for the complex, small-scale height variations around the measurement towers or close by canyons, it still provides useful location estimates for peak reflections in the radiometer's source area.

3. Spatial variability of reflected short-wave radiation

3.1. Observations

All four components of the net all-wave radiation were observed at KCL Strand. Their temporal variability and role in the surface energy balance in the dense urban study area are discussed in detail by

Kotthaus and Grimmond (2013). They also analyse how long-wave radiation is affected by a combination of atmospheric effects (cloud cover) and the urban surface, drawing on cloud cover fractions derived from ceilometer backscatter observations. Diffuse incoming short-wave radiation, measured with a sunshine pyranometer (SNP1, Delta-T Devices) over the period of Jan 2011–Mar 2012, has a clear relation to cloud cover fractions (not shown).

The urban impact on the observed radiation exchange is most apparent in the reflected short-wave radiation $K_\uparrow$ and hence the surface albedo. This is due to the immense heterogeneity of surface materials and geometry around the sites, which the following analyses illustrates.

The spatial distribution of reflected short-wave radiation observed at KSK (Oct 2008–Nov 2009; Fig. 2b) shows a clear response to objects in the source area of the down-facing pyranometer (Fig. 2a). Two flat roof windows south of the mast at KSK and a tilted roof window towards the southwest cause peak values of $K_\uparrow$. These appear as 'outliers' in the time series (Kotthaus and Grimmond, 2013, their Fig. 4). Averaged over a 15 m radius (80% FOV; solar elevation angle ⩽29.8°) for times with clear sky conditions, the roof windows at KSK have a 25% increase in albedo compared to the surrounding roof area which is composed of various kinds of concrete as well as slate roofing shingles. In addition to the marked roof window areas, the spatial distribution of reflected short-wave radiation reveals the influence of generally darker surfaces towards the east of the mast. This can be explained by the three-dimensional structure of the roof itself which casts greater shadow areas when the sun is in the east. At KSS the composition of the source area is more complex so that no isolated objects can be mapped. No windows are located on this roof.

The spatial variations of reflected short-wave radiation, and hence surface albedo, are evident under clear sky conditions as detected from ceilometer measurements. In order to study the effect of diffuse radiation in conjunction with the sun-surface geometry, median albedo patterns were calculated as a function of solar elevation angle and cloud cover at KSS and KSK (Fig. 3a and c). Those for clear (cloud cover = 0%) and cloudy (overcast, cloud cover = 100%) conditions were stratified by azimuth (easterly E, westerly W) and shown as a function of solar elevation angle (Fig. 3b and d). To facilitate comparison between figures (Fig. 2b, Fig. 3), the distance of maximum reflection of specular solar irradiance R_s (Section 2.3.2) is included in the upper x-axis in Fig. 3.
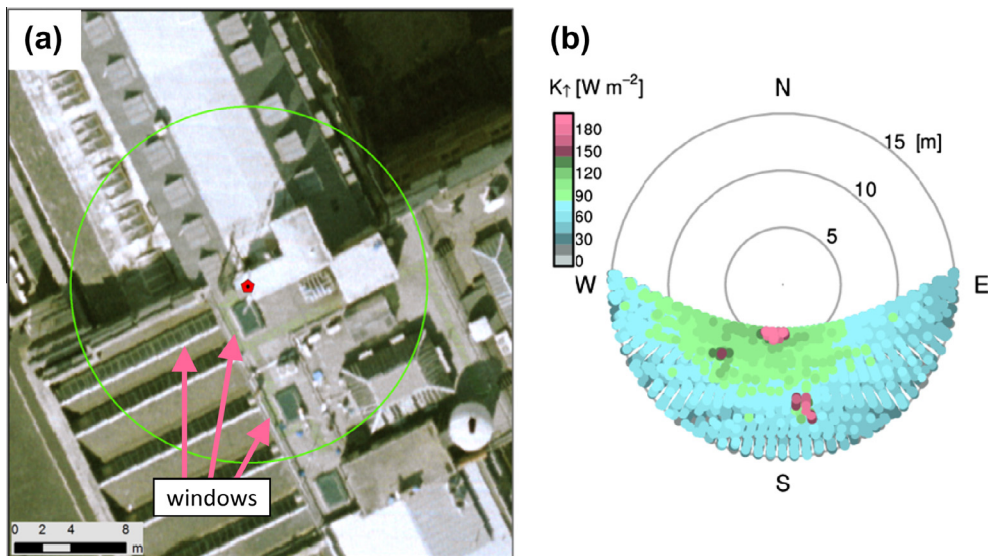

Fig. 2. (a) Aerial photo (NERC ARSF 2008) showing the 80% source area (15.2 m radius) of the down-facing radiometer at KSK; (b) median reflected short-wave radiation observed at KSK in 2009, by solar azimuth angle and distance of maximum, specular reflection R_s. Height above roof surface z_R = 7.6 m = tower height offset by 1 m (to account for roof height variations).
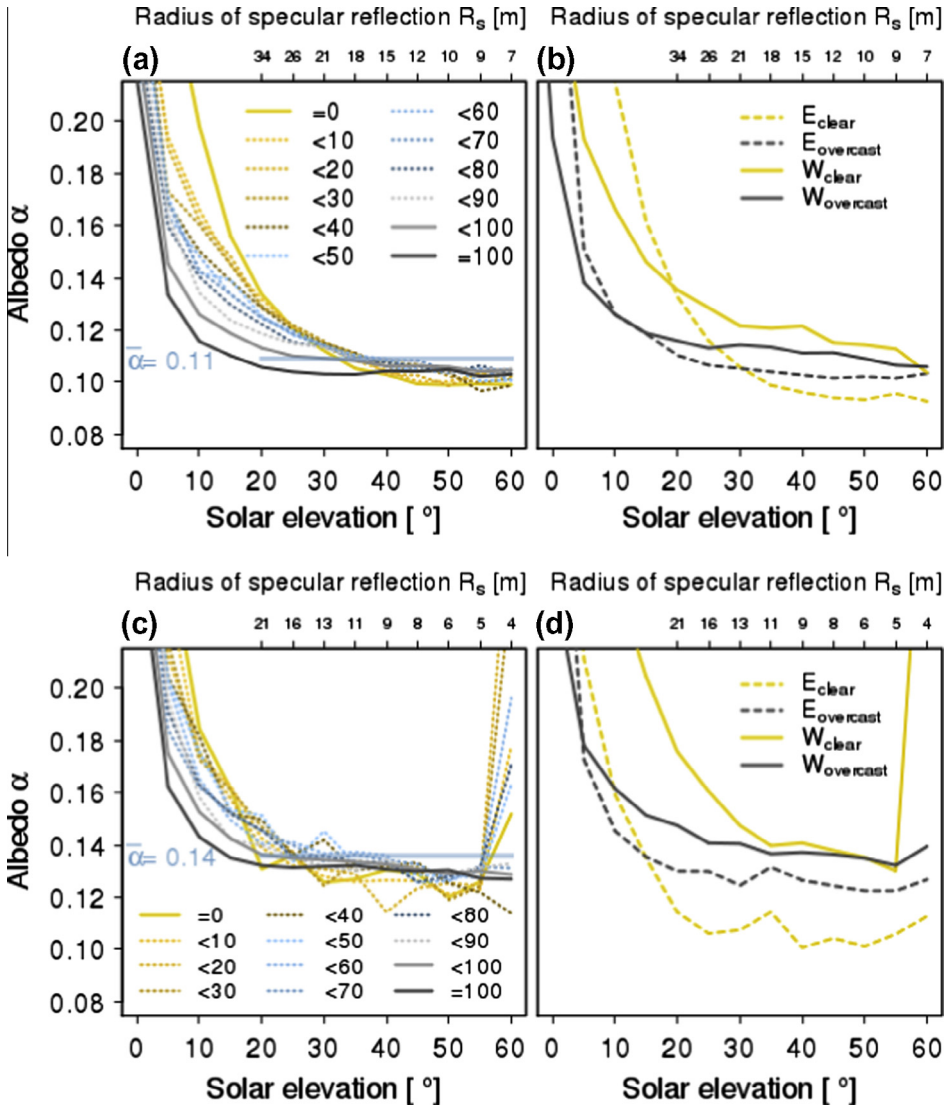
Fig. 3. Median surface albedo as function of solar elevation angle at (a, b) KSS and (c, d) KSK: (a, c) split by cloud cover [%]; (b, d) clear sky (cloud cover < 10%) and overcast conditions separated into E (sun in the East) and W (sun in the West). The bulk surface albedo $\bar{\alpha}$ is calculated as the mean of all values with a solar elevation angle of at least 20°. The additional axis (top) indicates the distance of maximum specular reflection of direct solar irradiance R_s from the respective tower location (see Section 2.2).

Cloud cover clearly affects the surface albedo estimates and determines its dependence on solar elevation angle (Fig. 3a and c), given the generally higher surface reflectance at low solar elevation angles results from increased specular reflectance. Accordingly, the surface albedo gradually decreases with rising solar elevation angle under clear sky conditions (0% cloud cover). The rugosity of the urban surface contributes to the lower albedo values at higher solar elevation angles as more short-wave radiation enters the street canyons (Christen and Vogt, 2004) where it is trapped. The slope of surface albedo versus solar elevation angle flattens with increasing cloud cover, especially for elevation angles

>20°. Surface albedo does not vary with solar elevation angle under overcast conditions (100% cloud cover).

At KSS (Fig. 3a), the gradient from clear to cloudy values is mostly evident for solar elevation angles below 40°, while those with higher elevation angles and hence lower distance to maximum reflection R_s become more similar. In contrast, at KSK (Fig. 3c), the overall albedo exhibits high variability for all but overcast conditions (i.e. cloud cover <100%). This could be explained partly by the smaller amount of data at this site (Kotthaus and Grimmond, 2013, their Table 1). However, since the fluctuation with distance to maximum reflection is stronger for times with more direct irradiance, it seems likely to be caused by high reflectance surfaces in the source area (Fig. 2). The window at $R_s \approx 5$ m southwest of KSK results in strong peaks of surface albedo. In addition to the high albedo surfaces, the presence of shadows increases the spatial variability of surface albedo under the influence of direct solar incoming radiation. Above 70% cloud cover, diffuse radiation gains importance and nearly removes the dependency on solar angles.

Despite the significant variability of albedo at the two sites and the uncertainties associated with measurements of this quantity, a bulk surface albedo can be estimated to summarise overall radiative characteristics. Here, it was calculated as the median of all observations with solar elevation angles of at least 20° (horizontal bar in Fig. 3a and c). As the larger source area for KSS included street canyons (to the north as well as to the southeast), the overall bulk surface albedo is lower ($\overline{\alpha} \approx 0.11$). Even though these observations did not cover the full range of facets in the area, this bulk albedo can be assumed to be more representative for the study area than the higher value of 0.14 measured at KSK where roof surfaces dominate. This again underlines the importance of sampling a representative composite of active urban facets to determine the radiation balance at the local-scale (Roberts, 2010). At both sites the bulk surface albedo is best represented by observations under overcast conditions. On average for solar elevation angle >20°, this white-sky albedo (diffuse radiation only) is a little lower (by 0.01) than the overall bulk albedo. The comparatively low albedo values observed in the current study (compared to e.g. Oke, 1987) are in accordance with the discussion of Christen and Vogt (2004) who found similar surface characteristics (albedo around 0.1 at their sites in the city centre of Basel) and concluded that European cities might reflect less short-wave radiation than those studied in North America.

Albedo observed under clear sky conditions changes with solar azimuth angle (simplified here into E and W) in response to the three dimensional geometry of the surface. At KSS (Fig. 3b) the surface appears brighter (for solar elevation angle >20°) when illumination comes from the west (W_{clear} in Fig. 3b) because flat roof surfaces made up most of the surface under the radiometer in a radius of about 20–30 m to the southwest of the tower (Kotthaus and Grimmond, 2013, their Fig. 1b). The canyon in the southeast, however, causes significant trapping of incoming solar radiation which lowers the observed surface albedo (E_{clear} in Fig. 3b). A small impact is even evident under overcast sky conditions ($E_{overcast} < W_{overcast}$ for solar elevation angle >20°), indicating that the canyon absorbs diffuse radiation as well. While the clear-sky albedo in the roof-dominated area (W_{clear}) steadily increases with decreasing solar elevation angle, the canyon-dominated area appears darkest at solar elevation angles around 50°. This sun-surface geometry corresponds to a distance to maximum reflection of about 12 m, which roughly marks the edge of the KSS roof towards the southeast and hence the place where minimal radiation escapes towards the sensor from the canyon. For smaller distances the influence of the KSS roof on the observed reflected short-wave radiation increases, and also more radiation reflected from the canyon reaches the sensor for larger distances.

At KSS, incoming short-wave radiation tends to be slightly lower in the morning hours (not shown) which could be a consequence of a not perfectly level sensor. Obviously this affects the observed albedo in addition to the surface structure in the source area. However, since a negative $K_\downarrow$ bias is associated with an overestimation of albedo, this (possibly measurement related) artefact acts to alleviative the observed E–W difference. Without this systematically higher incoming short-wave radiation for westerly solar positions the roof area would appear even brighter in comparison to the canyon. At the KSK site, no such asymmetry of incoming short-wave radiation with solar azimuth angle is detected. Again, clear-sky surface albedo is generally lower when the sun is in the east (E_{clear} Fig. 3d) where elevated roof structures cause apparent shadowing (Fig. 2a). The two roof windows detected (Fig. 2b) show up as distinct peaks in the median albedo curves of easterly ($R_s \approx 12$ m) and wes-

terly ($R_s \approx 5$ m) solar positions, respectively. Again, under overcast conditions, the high fraction of diffuse radiation integrates the diverse effects of the heterogeneous surface so that albedo at KSK shows hardly any variability ($E_{overcast}$ and $W_{overcast}$ in Fig. 3d) dependant on sun-surface geometry (for elevation angles >20°).

These observations demonstrate several important aspects characterising the urban surface and its anisotropic nature (also highlighted by Soux et al., 2004):

- High reflectance materials, which are increasingly found in modern urban architecture, significantly impact the surface albedo.
- Provided sufficient irradiance, these materials cause strong specular reflections or reflection glare.
- The surface deviates distinctly from Lambertian characteristics.
- Due to the heterogeneous composition of anthropogenic materials with various radiative properties, observations of the interaction between Sun, surface and atmosphere are highly dependent on the observational field of view or footprint (or source area).

3.2. Implications for source area models and siting

The anisotropic nature of the urban surface has implications for the description of radiometer source areas. The dependence of surface albedo on the relation between diffuse and direct illumination is linked to the spatial distributions of facets with different orientations in the source area. If the surface in the field of view of the radiometer covers walls and surfaces of a variety of orientations, and if these are similarly distributed by solar elevation and azimuth angles, the average albedo under clear sky conditions should be similar to the one observed during overcast periods (e.g. as seen at the central urban sites in Basel, Christen and Vogt, 2004) because both estimates represent an integration over a representative distribution of sun-surface-sensor geometry settings.

The source area (field of view) of a down-facing pyranometer over uniform, Lambertian surfaces is well described by concentric source area isopleths (Schmid, 1994). Here, the simple example of a highly reflective, forward scattering surface is considered to put the impact of the roof windows at the KSK site into a wider context.

Highly reflective, forward scattering surfaces in the pyranometer field of view can have enhanced impact on the observation of reflected short-wave radiation resulting in an overestimation of the local-scale flux if uniform source area weighting is applied. The latter is related to the distance of specular reflection R_s, and is dependent on the site latitude, the sensor height above the surface (in the current example the roof) and time (within year and day). To demonstrate this, R_s is shown for 70° N to 0° latitudes on the 21st of each month from June to December covering the range of possible solar positions (Fig. 4, reverse months for southern hemisphere and invert). For the northern hemisphere, the surface towards the south of the site influences the main part of the source area for specular reflections. The area from which specular reflection can reach the sensor for solar elevation angles ⩾20° (bold lines in Fig. 4) is closest to the tower at noon in June for latitudes down to 20° N. However, north of about 30° N the area right below the site does not contribute to any specular reflections. North of 50° N, specular reflections are only relevant for the period from March to September and a wider area can contribute during particularly long summer days.

The source area for specular reflections can be combined with the general field of view approach to ascertain which areas influence observations of reflected short-wave radiation. Using a site at 50° N (close to the KCL site latitude), the source area estimates are calculated with a sensor height of 5–30 m above the roof in 1 m intervals (Fig. 5). The FOV isopleths (dotted lines) do not vary with time, while the minimum distance of specular reflection (solid lines) depends on the day of year (same example days as in Fig. 4). The maximum distance reached (variable with time of day) is defined by the 20° solar elevation angle (grey shading marks the area of solar elevation angles ⩾20° where specular reflection can occur).

Comparison of the direct and diffuse footprint indicators illustrates that different surface areas can be important for the reflection of the two components of incoming solar radiation. Based on the fixed source area formulation (Schmid, 1994), it is possible to estimate the source area weighting of a flat 1 m^2 roof window at various distances from the site (squares in Fig. 5). The contribution is highest
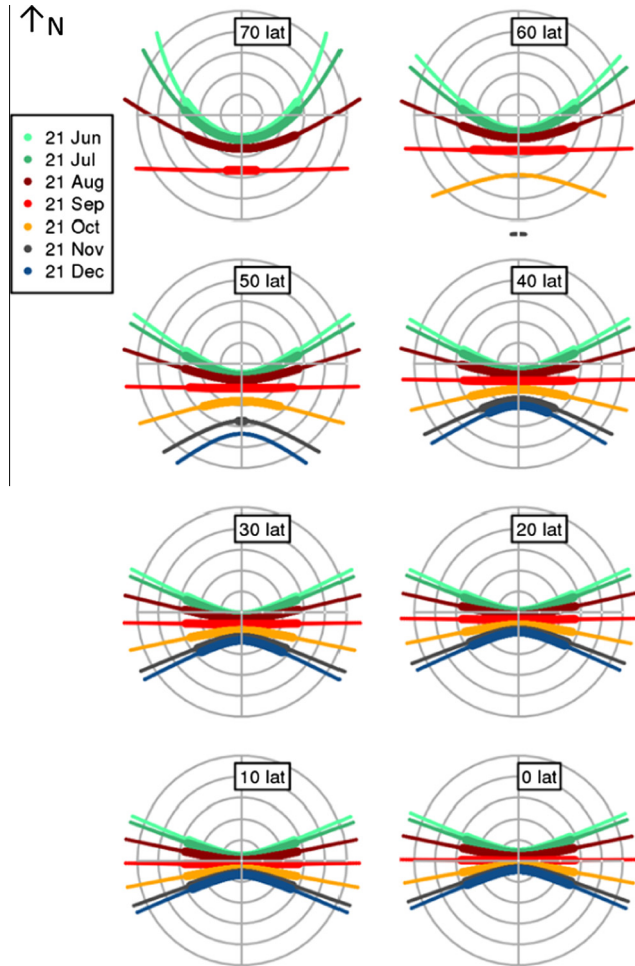
Fig. 4. Schematic illustration of location of maximum specular reflection at 0–70° N as a function of R_s (radial coordinate) and solar azimuth (angular coordinate) on the 21st of each month (Jul–Dec); for solar elevation $\geqslant 10°$ (solid lines), and $\geqslant 20°$ (bold lines). For the southern hemisphere the dates are reversed and patterns inverted.

for low measurement heights and decreases with increasing sensor height and distance from the site. However, highly reflective/non-Lambertian surfaces are most likely to influence observations of reflected short-wave radiation (Fig. 2; Fig. 3) at some distance from the site. For example, a radiometer at 15 m above roof level can receive specular reflections from a flat roof window 30 m south of the site from about March till September. Depending on site location and measurement time (Fig. 4; Fig. 5), a window at a certain distance from the measurement site and at a certain bearing could have a much higher impact on the final measurement than one located right below the sensor. Due to the spatial and temporal variability of specular reflection locations, the source area for clear sky albedo observations is more complex to parameterise than for times with diffuse radiation. A full source area model needs to describe variations in illumination conditions as well as the BRDF of the surface.

In the context of surface energy balance observations, the aspect of siting of a radiometer and the associated source area obviously also needs to be considered with respect to the source area of the turbulent fluxes measured (Schmid, 1997). It is a common issue for those observational datasets, that
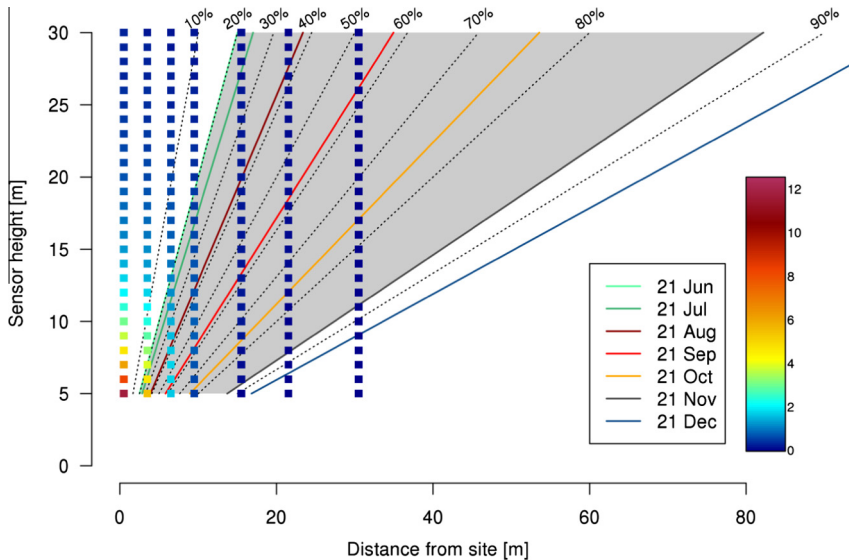
Fig. 5. Schematic of source area variations for a down-facing pyranometer depending on sensor height above roof and distance from site. Points give source area contribution of flat 1 m² roof window [%] according to concentric footprint isopleths (Schmid et al., 1991), indicated by dotted lines. Solid lines mark location of minimum radius of specular reflection R_s on the 21st of each month (Jun–Dec), calculated for a site at 50° N. See Section 3.2.

radiation sensors are often installed on top of the same towers as the EC sensors so that their FOV might only cover parts of the source area of the EC fluxes. At times, the footprint of radiative and turbulent fluxes might not overlap at all. Other than for studies of rural areas, where the observed surface is often sufficiently homogeneous to assume the radiative source area to represent the local-scale, outgoing radiative fluxes over the urban canopy may be affected by processes that may not be captured in the instantaneous source area of the turbulent fluxes, given the range of surface heterogeneities discussed. Hence, in addition to an improved understanding of the radiometer source area, new approaches in terms of siting might be advisable in order to ensure that a representative composition of facets is captured (Roberts, 2010). Ideally radiometers would be mounted higher than turbulence sensors (Offerle et al., 2003; Roberts, 2010). Often this may be unrealistic because of planning restrictions. Hence, an increased number of radiometers installed in various directions (e.g. predominant wind directions) could potentially provide a better spatial coverage. Obviously, with advances in surface remote sensing (Yang, 2011), both in terms of spatial resolution and temporal coverage, observations from other non-tower based platforms might help to quantify radiative fluxes in the future, but these need to be viable across all cloud conditions.

4. Spatial variability of turbulent heat fluxes

4.1. Wind and surface morphology

Around the KCL Strand campus the morphology is complex (Fig. 1), street canyons dominate to the west and north, whereas to the south the River Thames has significantly lower surface roughness. This diversity impacts the roughness parameters: plan area fraction λ_p, frontal area index λ_f, mean building height z_h, roughness length for momentum z_0 and zero plane displacement height z_d (Fig. 6a and b).

On average (Table 1), the KSS measurement height ($z_m \approx 2.2 \times z_h$) should be above the blending height, whereas the KSK observations may be within the roughness sublayer ($z_m \approx 1.9 \times z_h$). Still, based on morphometric parameters alone, it is difficult to locate the blending height. Hence it is

not certain if/when observations at KSK rather represent the roughness sublayer. In Basel (Rotach et al., 2005) during the BUBBLE campaign, multiple levels of EC instruments on two urban and one suburban flux tower provided information about vertical variations in turbulent exchange from within the canyon up to a local-scale fetch (Christen, 2005). Based on the vertical divergence of the sensible heat flux density at a central urban BUBBLE site, Christen and Vogt (2004) conclude that the main influence on measurements at the top (2.2 times the mean building height z_h) originates from the volume around roof height (>$0.8 \times z_h$ and <$1.4 \times z_h$). Their findings also suggest that the blending height in the dense urban setting is reached at about $1.5 \times z_h$, above which vertical flux divergence vanishes.

At the two study sites, the mean building height is higher (lower) towards the northwest (southeast) with median values in the west and east (Fig. 1, Fig. 6a and b). The directional plan area fractions are clearly impacted by the river with $\lambda_p < 0.45$ in a sector 85–245° (85–235°) at KSS (KSK). The variability in displacement height z_d is primarily controlled by mean building height, and then λ_p (Macdonald et al., 1998). Thus it is reduced in the south to southeast, with a z_d/z_h minimum of 0.42 (0.36) at 180° for KSS (KSK). As all these components are required for the roughness length calculation (Section 2.3.1), z_0 varies between 1 m at KSS (0.8 m at KSK) and 2.8 m. Surface roughness is particularly high in the southwest and northwest, while the relatively high displacement height (compared to
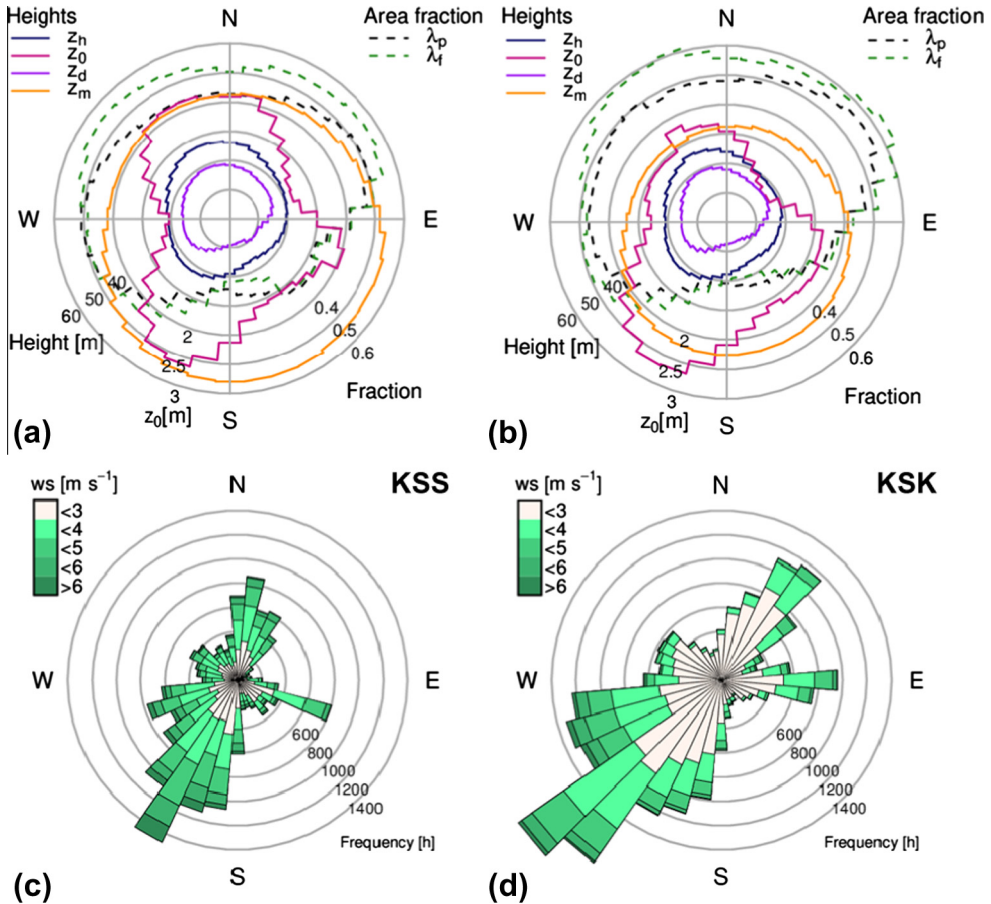

Fig. 6. Directional characteristics at (a, c) KSS and (b, d) KSK, separated into 10° intervals: (a, b) Average surface characteristics based on individual source areas maps: Building height z_h, roughness length z_0, displacement height z_d and measurement height z_m, plan area fraction λ_p and frontal area fraction λ_f. (c, d) Frequency distribution of wind speed by wind direction.

z_h) in the west and east lowers the surface drag. Roughness estimates for KSK and KSS are generally in agreement by direction, but the lower measurement height at KSK causes a small/different footprint (Section 4.2). This may explain why the clear increase in surface roughness to the north is evident for KSS (Fig. 6a) but less pronounced for KSK (Fig. 6b). In addition to the diversity of surface roughness elements in the study area, the underlying topography (Fig. 1) adds complexity to the source area calculations. As it is not flat, the measurement height z_m was calculated as a function of wind direction (Section 2.3.1).

The wind-rose, based on all available EC observations (Section 2.2), shows which wind sectors are most frequently observed by the flux sites. The prevailing wind direction (45% of all observations) at KSS is from the southwest (175–265°; Fig. 6c); the secondary sector (18%) is the opposite from the northeast (355–45°). As the measurements at KSK (Fig. 6d) cover a longer period (Kotthaus and Grimmond, 2013, their Table 1), the absolute frequency values are higher than for KSS. Although the two dominant wind sectors can be identified for KSK, they are slightly shifted towards the west (southerly) and east (northerly), respectively. Given the KSK sensor height was lower (Table 1) surface roughness elements in the immediate surroundings can impact the observed turbulent flow and thus the dispersive fluxes (Raupach and Shaw, 1982) might have an influence. The northeast–southwest oriented building north of KSK (i.e. the one hosting the KSS site, Fig. 1) likely caused sheltering effects and thus explains the difference in wind direction distribution compared to KSS. The wind speed distribution (shading in Fig. 6c and d) corroborates this observation. Higher wind speeds occurred at the higher KSS sensor (61% of all observations with $\geqslant 3$ m s^{-1}) and a stronger decelerating effect of the surface roughness is seen at KSK (62% with $\leqslant 3$ m s^{-1}). At both sites, stronger winds occurred from around 240° where more than 60% (50% at KSK) of the data show wind velocities >3 m s^{-1}.

Further, frequencies are slightly higher between 105° and 115° (Fig. 6c) with about 4% of all observations. These directions coincide with the alignment of River Thames to the east of the site (Kotthaus and Grimmond, 2013, their Fig. 1), indicating that channelling might impact the flow from this direction. These easterly wind directions, however, are often coincidently observed at London airports (e.g. Heathrow, City, and Luton, Met Office, 2012a; not shown), which probably rules out them being induced by local-scale, site specific flow distortion by the urban canopy in the site's source areas.

4.2. Modelled source areas of turbulent fluxes

The local-scale source areas, estimated for each observation period using Kormann and Meixner's (2001) model (Section 2.3.1), have uncertainties caused by the complex environment that need to be kept in mind during interpretation. The spatial variability of roughness elements by direction for each EC site (Fig. 6a and b) was used to calculate the appropriate morphometric parameters and roughness characteristics (Section 2.3.1) for each individual time period's source area. Atmospheric stability plays a major role in the determination of source area locations (Kormann and Meixner, 2001), the footprint area increases with increasing stability as does the distance from the site to the maximum footprint contribution. At KSS (KSK), atmospheric conditions are predominantly unstable (neutral), with about a third (60%) of all observation periods classified as neutral. At both sites, stable stratification is rarely observed (Kotthaus and Grimmond, 2013). The overall source area characteristics of both sites are listed in Table 1.

Here, the KSS site results are analysed for neutral and unstable atmospheric conditions. Through aggregation of the individual source area weights (Fig. 7a and b) a footprint climatology has been derived. Wind direction distributions differ slightly for the two stability regimes, as is reflected in the overall shapes of the source areas (compare Fig. 7a and b, see, for example, such as the low probability of south-easterly flow under neutral stratification). A larger (smaller) surface area influences the flux observations under neutral (unstable) conditions with the area contributing 50% to the footprint (shading in Fig. 7a and b) extending on average to about 410 m (250 m) to the southwest and 330 m (180 m) to the northeast. To determine the average surface composition influencing exchanges, the individual source areas were used to weight the land cover fractions in 10° sectors using the individual 30 min mean wind direction (Fig. 7c and d). Consistently, vegetation (e.g. grass and shrubs) and trees (here counted separately) are a small portion of the source area (Table 1) with maximum coverage (total of 11%) towards the east. Here, a small park (*Temple Gardens*, Fig. 1) and street trees are located within

the 80% footprint isopleth (Fig. 7a and b). Generally, impervious surfaces dominate with buildings and roads forming more than 80% of the source area (Table 1). Roads have a slightly larger plan area than buildings, except to the northeast where this is reversed. For the west to northeast (245–55°), where impervious surfaces make up more than 90%, surface cover fractions within the source area show little difference with atmospheric stability. Given the vicinity of the River Thames (Fig. 1), open water contributes to the source areas in a broad sector between 75° and 245°, with substantial fractions (>40% for unstable conditions) from 105° to 205°. To the northwest, the maximum source area contribution (not shown) aligns with a major road (*The Strand*, Fig. 1) where anthropogenic heat emissions from traffic are expected to be substantial (Iamarino et al., 2012). The overall source area climatology indicates a strong influence from the *Aldwych* junction (Section 2.1) at the 50% level (Fig. 7a), again with shorter extent for unstable conditions.
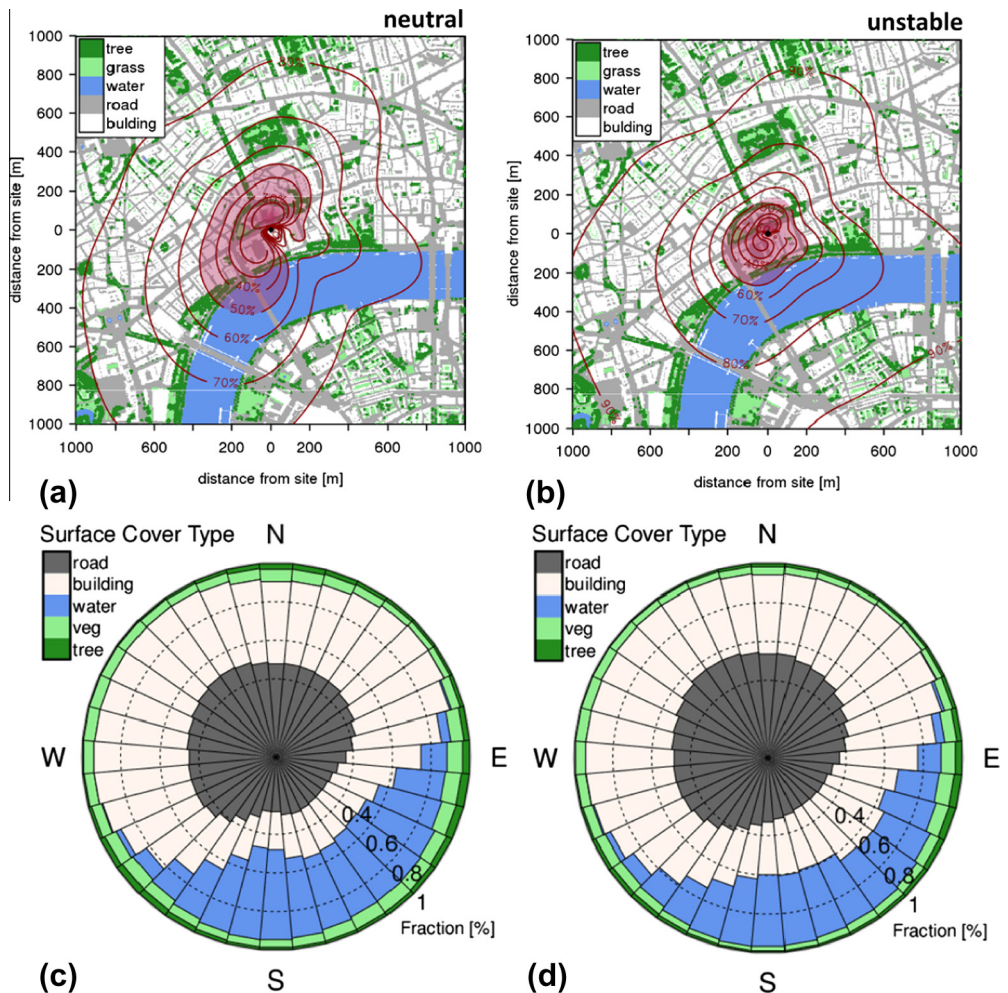

Fig. 7. Spatial and directional characteristics at KSS for (a, c) neutral and (b, d) unstable atmospheric stability: (a, b) Accumulated source area weights. Area contributing up to 50% of the source area is shaded. Underlying map of land cover types, 4 m resolution (based on OS MasterMap and vegetation data from Lindberg and Grimmond 2011). Maps are centred on the tower. (c, d) Accumulated surface cover fraction per 10° intervals, normalised by total amount of observations within each interval.

For northerly wind directions, some influence from traffic emissions can be expected. However, for the prevailing wind direction from the southwest (Section 4.1), source area characteristics are very diverse. The climatological 50% isopleths include a large pedestrian courtyard (*Somerset House*, Fig. 1), busy roads (*Waterloo Bridge*), and many tall buildings alongside open water (*River Thames*). This diversity complicates the interpretation of turbulent surface exchange based on the modelled source area.

In general, the modelled fetch at KSK (not shown) does not reach as far and has a slightly different alignment (as expected from the wind rose comparison in Fig. 6). This shift of the wind roses in conjunction with the slight spatial displacement of the two sites of about 60 m (Kotthaus and Grimmond, 2013) can result in situations where the eddies observed at the two sites might have been influenced by quite different sinks and sources. Especially for unstable conditions, when source areas are small, observations at the KSK site might have been affected more by nearby roofs and canyons rather than a footprint at the local-scale. Still, even in the roughness sublayer, fluxes are related to surface controls. For example, Kanda et al. (2006) investigated the spatial variability of turbulent fluxes in the roughness sublayer during a winter period where sensible heat flux observations from sites influenced by different source areas were successfully explained by variations in vegetation surface cover. On average, the 50% isopleths for KSK do not include the river towards the south (potential moisture source) and only a small fraction of the busy *Aldwych* junction (potential heat source). The modelled source areas for KSK are probably inappropriate for the times that the measurements are within the roughness sublayer as the fundamental assumptions of the footprint model are not fulfilled. Thus, the footprint analysis (Section 4.3) is concerned with the KSS site only.

4.3. Analysis of footprint surface-atmosphere exchanges

Based on source area characteristics, the relation between surface forcing and observed energy exchange is examined. The turbulent latent and sensible heat fluxes clearly have variations at seasonal and diurnal scales (Kotthaus and Grimmond, 2013, their Fig. 6), which, combined with systematic temporal variations in wind direction (for example, northerly winds were more frequent during winter months, not shown), could potentially confuse the investigation of surface controls. In order to minimise this effect, turbulent fluxes were normalised by the incoming radiative fluxes ($Q_\downarrow = K_\downarrow + L_\downarrow$). Median energy flux ratios $Q_H/Q_\downarrow$ and $Q_E/Q_\downarrow$ are analysed by wind direction (aggregated into 10° intervals) and surface cover percentage (Fig. 8). Furthermore, precipitation clearly affects the Bowen ratio (Kotthaus and Grimmond, 2013, their Fig. 9) and is most often associated with frontal systems of mid-latitude cyclones approaching London from the southwest (Met Office, 2012b). Hence, fluxes are shown for all conditions (all, Fig. 8) and restricted to measurements with no rainfall within the preceding 12 h (dry) in order to alleviate a potential directional bias caused by precipitation.

Sensible heat flux (Fig. 8a) is strongest from 205° to 85°, where median Q_H usually makes up at least 22% of $Q_\downarrow$, compared to southerly and southeasterly directions, where most median estimates are below 20% $Q_\downarrow$. In the first instance, this contrast reflects variations in surface cover characteristics given the energy flux ratio is higher in areas where impervious surfaces dominate (>80%). However, a series of variations can be identified which illustrate that surface controls on the fluxes are more complex and not driven by the surface cover types alone. For instance, areas with almost complete impervious cover (>90%) are not associated with higher fluxes than those with small amounts of vegetation (80–90% impervious). Rather, the flux ratios are highest for the latter in an area north of the site between 335° and 45°. Furthermore, even very low median values of Q_H (<10% $Q_\downarrow$) occur for periods with dominant impervious fractions in the flux source area, namely between 105° and 145° and 165° and 205°. Sensible heat flux ratios within these two wind direction regions do not indicate a clear response to surface cover fractions of roads and buildings (ranging from 40% to 100%), rather they are constantly low. These directional patterns, both to the N and to the SE/S, suggest that other effects, besides the impervious surface cover fractions, need to be considered when interpreting the fluxes observed.

The impact of surface roughness variations in the complex CBD setting can be expected to account for some of the directional patterns seen in the energy flux ratios (Fig. 8). The surface drag is reduced for wind directions aligned with the River Thames (not shown), i.e. in the south (185–205°) and the southeast (115–140°). Wood et al. (2013) found enhanced flow relative to the flux tower sites along the river at this location. Horizontal gradients of temperature and moisture (such as seen in Marseille,
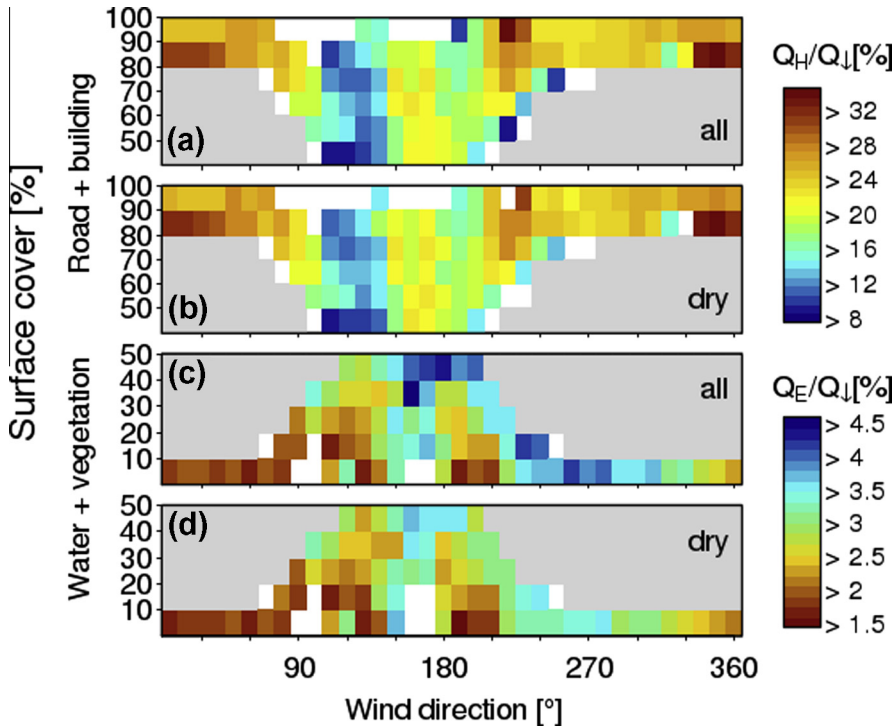
Fig. 8. Median heat flux (a, b) Q_H and (c, d) Q_E at KSS normalised by incoming radiation $Q_{\downarrow}$ by wind direction and surface cover; (a, c) all conditions; (b, d) restricted to periods with no rain within the preceding 12 h. Minimum number of measurements available to calculate the median for each interval (a, b) 15; (c, d) 20 (white – insufficient data). Grey shading indicates land cover/wind direction combinations that cannot occur.

Pigeon et al., 2007) could play a role. These regions coincide with those of reduced sensible heat flux (Fig. 8a and b) which suggests that variations in turbulent statistics and momentum transport could explain some of the variability of the turbulent latent and sensible heat fluxes observed. However, given the complex nature of the area surrounding the site, a comprehensive analysis is required to understand the nature of turbulence influencing these measurements. This is beyond the scope of the current study and will be presented elsewhere. These turbulence characteristics may, however, indicate that the reduced sensible heat fluxes (and momentum fluxes, not shown), especially from SE directions, are also associated with larger scale advection which single EC towers are not able to capture. In cases of horizontal advection, the fluxes observed are driven by spatial differences in local-scale surface controls which are not well addressed in the commonly applied EC source area models (Section 2.3). The fact that normalised sensible heat fluxes do not seem to respond to the amount of impervious surface cover estimated by the footprint model, could suggest that the observed fluxes indeed do not represent the calculated local-scale source area from directions 105° to 140°.

Modelling approaches incorporating the three dimensional nature of the surface (possibly with back trajectories) would be required to understand the 'history' of the observed atmospheric conditions. Advection has long been recognised to impact EC observations under complex conditions (e.g. Aubinet et al., 2003). Still, there are no simple tools to address the issue of advection (e.g. Feigenwinter et al., 2008; Aubinet et al., 2010). Typically extensive observations are required to be combined with numerical modelling (e.g. Pigeon et al., 2007). Ideally, EC sites should be installed where advection effects are minimal. This requirement, however, is difficult to meet when studying the patchy urban landscape, with areas of varying building density interspersed with areas of very different materials (e.g. parks, rivers and lakes). Advection effects caused by these characteristic urban components need

to be addressed during the observation and modelling of urban climate conditions. As cities are retro-fitted and built to be more "livable" this patchiness will likely increase further. Thus there is a need to develop appropriate tools to ensure that measurements are appropriately understood and that model performance is evaluated adequately before being utilised for decision making.

In addition, there are meso-scale effects that influence the meteorological conditions observed in central London when the flow is coming from the east. As seen in the KSS wind rose (Fig. 6c), about 4% of the observations are from around 110°, which aligns with the River Thames. Tidal effects might affect the overall roughness of the urban area of Greater London as a whole. Moreover, this wind direction is associated with sea breezes (Bohnenstengel et al., 2011; Chemel and Sokhi, 2012). Further investigation is required in order to understand the relation of local-scale surface controls and synoptic scale conditions as forcing for the observed turbulent surface fluxes.

Overall, the impact of precipitation and associated wet surfaces is not particularly strong on the sensible heat flux (Fig. 8b). On some occasions rainfall results in a reduced Q_H, mostly for the region 190–250°, but this sector already had smaller heat fluxes. As expected, the moisture input has a much stronger influence on the latent heat flux (Fig. 8c and d). For southerly and westerly flow, which represent typical conditions for frontally induced precipitation in the UK, the occurrence of $Q_E > 3.5\% \, Q_\downarrow$ is obviously higher when the urban fabric is wet. Still, even when those times are excluded from the analysis (Fig. 8d), the latent heat flux shows a clear signal of higher fluxes from a broad south-westerly range of wind directions (150–280°). This could be an artefact of the way 'dry' surface conditions are defined here. Possibly, the effect of increased evaporation fluxes due to moisture supply by wet surfaces after rainfall occurs for more than 12 h, even though its impact on the Bowen ratio clearly decreases after this period of time (Kotthaus and Grimmond, 2013). This is not surprising, given the turbulent flux of latent heat observed in this CBD is considerably smaller than that of sensible heat, so the impact on Q_E needs to be substantial to show up in the ratio of energy partitioning. No effect of rainfall is detected under northerly wind conditions where median normalised evaporation is consistently low (<2.5% $Q_\downarrow$).

As for the sensible heat flux, the relation of latent heat flux ratios to surface cover fractions in the source area is complex (Fig. 8d). Median latent heat fluxes range between 2% and 3.8% of $Q_\downarrow$ over the whole range of vegetation and water surface cover (0–50%). Very low fluxes (<2% $Q_\downarrow$) occur for some areas where those surface fractions make up less than 30%. The river, which according to the footprint analysis (Fig. 7c) contributes significantly to the source area between 105° and 205°, does not have a distinct signature in the latent heat fluxes. It could be argued that the open water surface supplies moisture for evaporation in a region between 175° and 215° where the latent heat flux ratio appears to indicate an increase of fluxes with water (+ vegetation) surface cover. However, given that the wind directions of increased rainfall and considerable open water surface cover overlap, it is not possible to separate the impact of the two surface moisture sources completely (based on the data available).

In addition to the surface cover types, the three dimensional structure of the surface can give insight into mechanisms governing surface controls on the evaporation flux observed. The river introduces rather abrupt changes in surface roughness (Fig. 1) to the urban canopy which presumably initiate internal boundary layers (IBL) at the river banks. Thermal effects driven by the temperature differences between the water body and the urban fabric may play a role at times. Given the vicinity of the site to the open water surface (<200 m) and the relative height (59.1 m above sea level, tides ±3 m), the IBL characterised by the river might be too shallow to reach the sensors. Extensive measurements and/or a high-resolution model would be required to capture the nature of this potential IBL. According to a simple parameterisation (Elliott, 1958; assuming a roughness length of 0.1 m for the river surface which includes boats etc.), an IBL initiated at the rough-to-smooth transition at the south bank of the river would probably develop to a height of 35–50 m when reaching the north bank (river width ≈300 m). Therefore the IBL height would remain below the KSS measurement level under southerly flow directions. Thus the surface characteristics south of the river would impact the sensor which may explain the lack of large increase in latent heat flux from these directions. Source area models currently available for the interpretation of EC fluxes, such as the analytical model used here (Section 2.3.1), are not able to capture such complex structures.

Vegetated areas add complexity to the interpretation of potential moisture sources for the maintenance of latent heat fluxes. These may also contribute to prolonged moisture supply after rainfall. Overall, urban vegetation has a comparatively small presence and no large variations with wind direction (Fig. 7c). There are a few more street trees immediately north of the site and slightly more trees and vegetated areas beside the riverbanks (e.g. Temple gardens), but their close proximity to the open water makes it very difficult to separate their effect on the observed surface energy exchange. Further, the small magnitude of the turbulent latent heat fluxes observed in this dense urban environment may mean that the differences between fluxes from certain wind directions are within the observational uncertainty of eddy covariance. Still, despite the small magnitudes of the latent heat flux ratios with incoming radiative energy, the analysis (Fig. 8c and d) suggests that rainfall is the most important moisture source for evaporation in the CBD studied.

The variations of both turbulent fluxes presented suggest that surface cover type alone does not characterise sufficiently the surface controls on surface energy exchanges, rather the impact of surface roughness seems to be significant at various scales. Further aspects to be considered are the spatial patterns of the storage heat flux and the locations of anthropogenic heat and moisture sources in the CBD which are not necessarily captured in the map of land cover types used for the current footprint analysis (Fig. 7a). For example, the latter does not account for the potential effect of anthropogenic moisture sources in areas of impervious land cover (Kotthaus and Grimmond, 2012) and does not distinguish between busy roads and pedestrian areas (e.g. the *Somerset House* courtyard). For this reason, auxiliary data from an anthropogenic heat flux model (Iamarino et al., 2012) have been incorporated into the energy balance analysis for the current study area (Kotthaus and Grimmond, 2013) as an attempt to account for anthropogenic activities around the site. Kotthaus and Grimmond (2013) use source area estimates from this study to spatially align the modelled flux with the EC observations.

4.4. Inter-site comparison

Instruments at KSK were lower than at KSS (Table 1), hence the roughness parameters (Section 4.1) and source area characteristics differ. As the KSK measurements were within the roughness sublayer at times, the immediate surroundings (buildings and canyons at KCL Strand) would have strongly influenced the turbulent surface exchanges observed. Evidence of the impact of the surface roughness elements on the flow at KSK has been found in the wind direction frequency distribution, as it is shifted relative to that observed at KSS (Section 4.1, Fig. 6). Thus to compare simultaneous observations at the two sites, the analysis here is based on the KSS wind direction (dir_{KSS}) and the deviation observed at KSK ($dir_{KSS}–dir_{KSK}$; Fig. 9). As the simultaneous measurements of latent heat flux observations are limited (Kotthaus and Grimmond, 2013, their Table 1), and the flux is generally of small magnitude, Q_E is not plotted. The shaded area ($dir_{KSS} \approx 39–97°$) marks the region where micro-scale anthropogenic emissions have been detected at KSS (Kotthaus and Grimmond, 2012) or flow distortion induced by the instrumental setup (sensor mountings) might have occurred. No obvious distortion effects are evident in this region of wind direction. However, given the frequency of observations from this sector is low and further diminished due to quality control restrictions (Kotthaus and Grimmond, 2012), it is not discussed in the comparison of KSK and KSS observations. No numerical requirements have been applied to the observations in each wind direction bin, in order to display the full range of observations (Fig. 9a). However, this should be considered in the analysis of the median ratios of the atmospheric variables (e.g. wind speed, Fig. 9a). From the observed wind roses (Fig. 6c and d), it is evident that KSK wind is slightly distorted to the right (resulting in higher wind direction values compared to KSS) for winds from the southwest and northeast and to the left (lower wind direction values) from the west/northwest and east/southeast (Fig. 9). Despite precise instrument-alignment and assessment against an independent reference (wind direction observations at London Heathrow Airport, Met Office, 2012a) some of the deviation may be related to measurement inaccuracies. However, as both negative and positive deviations are detected a simple bias due to misalignment does not explain the differences.

Wind speed, friction velocity and surface drag coefficient ($C_D^{1/2} = u^*/U$) give useful insight into the influence of roughness elements on the observations at KSK when put into relation to those at KSS (Fig. 9b–d). These variables are discussed first, in order to provide the context for interpreting the
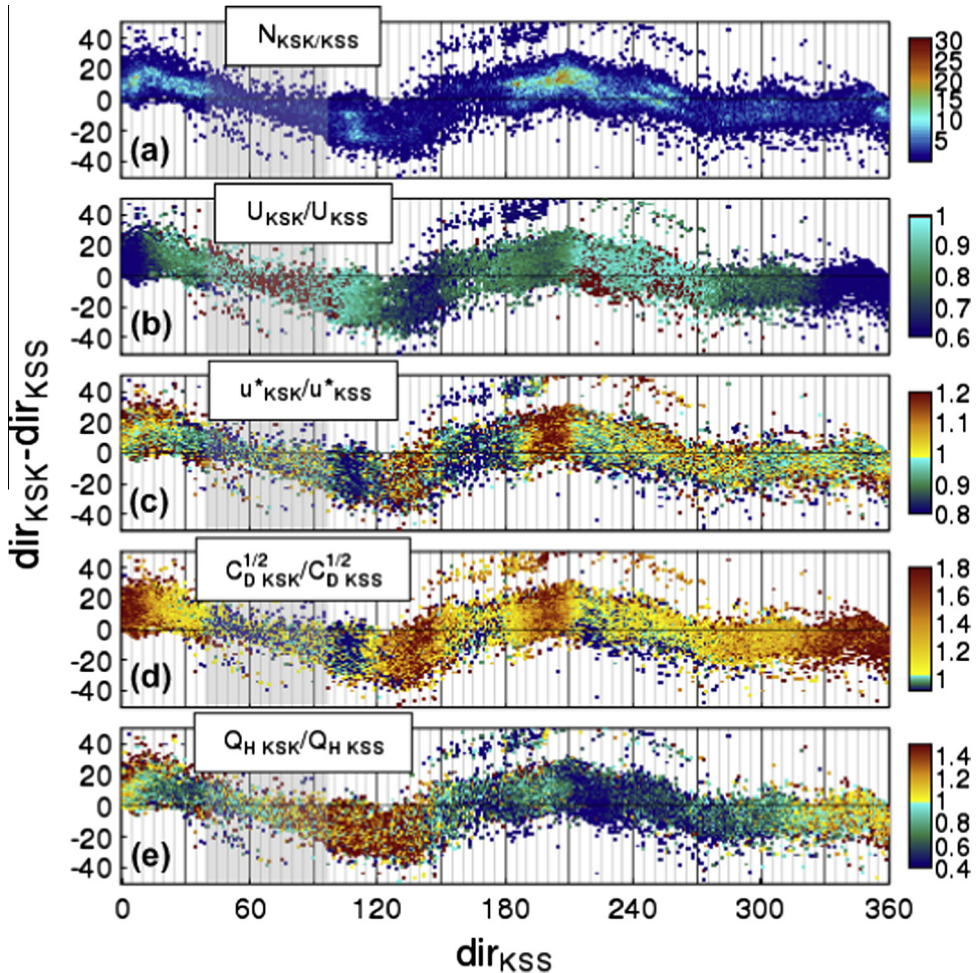
Fig. 9. Median ratio of observations at KSK and KSS of (b) wind speed U, (c) friction velocity u^*, (d) drag coefficient $C_D^{1/2}$, and (e) sensible heat flux Q_H by KSS wind direction and the deviation of wind direction at KSK from that at KSS; (a) the number of measurement periods analysed is shown for wind speed ratio (b). $\mathrm{dir_{KSK}}$–$\mathrm{dir_{KSS}}$ is restricted to an absolute deviation of 50°. (grey shading; 39–97°) Sector affected by micro-scale anthropogenic sources (IMAS; Kotthaus and Grimmond, 2012) at KSS and potentially flow distortion effects from the mountings.

sensible heat flux patterns (Fig. 9e). As the wind roses (Section 4.1) showed, overall winds are stronger at the higher measurement level at KSS (Fig. 9b). Friction velocity is often of similar magnitude at the measurement locations (Fig. 9c); however, there are regions where u^* values observed at one clearly exceed those at the other. The surface drag coefficient is generally higher at KSK (Fig. 9d) with only two exceptions, i.e. wind directions 100–115° and partly around 225° ($\mathrm{dir_{KSS}}$).

The most consistent and 'homogeneous' fetch for the two EC sites at KCL is located in the north to north-westerly directions (Fig. 7c and d). Here, height variations have presumably less impact than to the south (Fig. 1). For a broad range of wind directions ($\mathrm{dir_{KSS}} \approx 280$–40°) wind speeds are, as expected, considerably higher at KSS (Fig. 9b), thus the lower surface drag coefficient (Fig. 9d) at this higher measurement level. From these directions, the flow observed at the two sites appears to be systematically related. Wind speeds at KSK are, on average under neutral conditions, 0.6 (330–10°) to 0.7

(285–320°) times lower. This suggests a slightly stronger increase of wind speed with height/wind shear than would be described by a neutral logarithmic wind profile. From this, mean wind speed at KSK should be about 0.8 times that at KSS (for $dir_{KSS} \approx 330–10°$ as well as $dir_{KSS} \approx 285–320°$) for neutral stratification periods using the first order roughness parameters (Section 4.1). Hence, it could be argued that observations from these wind directions represent conditions similar to the well-blended surface layer. This agrees with the dense urban canopy in this fetch which makes skimming flow more probable so that mixed turbulence could be observed, even though from these directions both measurement levels are probably below the rule of thumb estimate ($2 \times$ the mean building height) of the blending height (Section 4.1). These findings support the expectation that in densely built areas the blending height will be lower (e.g. Mulhearn and Finnigan, 1978; Raupach et al., 1980), as seen in the observations of Christen and Vogt (2004). It further underlines the need to evaluate morphometeric parameterisations under these conditions.

A small sector of wind directions (around $dir_{KSS} \approx 110°$), apparent in both wind roses (Fig. 6c and d) and discussed in the footprint analysis of KSS observations (Section 4.3), indicates channelling by the nearby river. Here, the KSK wind speed has a local maximum so that observations are very similar to those at KSS (often $U_{KSK}/U_{KSS} > 0.9$). Wind directions of $dir_{KSS} \approx 100–115°$ represent the only region where both friction velocity and surface drag coefficient are clearly higher at KSS compared to KSK, with ratios of about 0.8 and 0.9, respectively. The DEM around the sites (Fig. 1) shows the ground and building height variations at KCL Strand. The orientation of the building hosting the KSK mast, suggests that bluff body effects could influence the flow observed at this lower measurement height towards the southeast. Further, flow is potentially separated to bypass the bluff body, which would introduce wake flow into the turbulence observed at KSK. This bluff body might cause acceleration of the flow around it, explaining the relatively higher wind speeds, reduced friction velocities and surface drag discussed for directions of $dir_{KSS} \approx 100–115°$ (Fig. 9b–d).

As noted (Section 4.3), the surface drag and u^* observed at the higher KSS tower (not shown) are reduced for wind directions aligned with the River Thames ($dir_{KSS} \approx 115–140°$ and $185–205°$). Friction is higher for the region in between ($dir_{KSS} \approx 155–175°$), where the fetch of open water is considerably smaller and the sharp increase in surface roughness at the north bank of the River Thames might cause some bluff body-type impacts on the flow from these directions. The u^* variation at KSS is evident in the observed ratios (Fig. 9b and c). The intra-site comparison (Fig. 9) has the bluff body effects of the KSK building (possibly affecting the flow for $dir_{KSS} \approx 100–195°$) and the river-roughness variations seen at KSS ($dir_{KSS} \approx 110–210°$) superimposed. For example, to the west of KSK, increased wind speeds and decreased surface drag may be expected, similar to those at $dir_{KSS} \approx 100–115°$, but they are obscured by the KSS signature (Fig. 9b–d).

Wind speeds at the two heights are similar between $dir_{KSS} \approx 210–280°$ (Fig. 9b): the median ratio of observations at the two locations is close to unity and some KSK wind speeds are even slightly higher than those at KSS (maximum $U_{KSK}/U_{KSS} = 1.01$; cf. compared to the mean of 0.9 for neutral conditions calculated using the log-law based on average initial morphometric parameters for all directions). These south-westerly directions are probably where the KSK tower encounters the least roof-induced roughness in the immediate surroundings and the flow observed at KSS is influenced mainly by roads and buildings (rather than the open water). The surface drag is mostly higher (factor of ≈ 1.2) at the KSK site (Fig. 9d). However, the stronger winds at KSK (Fig. 9b) for some wind direction combinations impact the surface drag coefficient (Fig. 9d). In the south-westerly region, wind speed (Fig. 9b) and friction velocity (Fig. 9c) variations are correlated with the wind direction deviations ($dir_{KSK} − dir_{KSS}$, Fig. 9), but the ratio of friction velocity in this region is very complex. Again, a more in-depth analysis of turbulence characteristics might lead to a better understanding of processes governing the flow from these directions observed at the two heights.

Within $dir_{KSS} \approx 280–40°$ there are low wind speed ratios to the north ($dir_{KSS} \approx 325–10°$; Fig. 9b) potentially caused by bluff body effects. The KSK tower is only 1.5 m taller than the building hosting the KSS tower (Fig. 1), so flow distorted around this building from both its westerly and easterly sides, affects the deviations at $dir_{KSS} \approx 280–320°$ and $dir_{KSS} \approx 10–40°$, respectively. Winds observed at KSK are slightly accelerated compared to the northerly region ($dir_{KSS} \approx 325–10°$) as is evident in the wind speed ratio (Fig. 9b). Given the southwest–northeast orientation of the building (Fig. 1), the edge effect

is sharper at the easterly end, where the redirection of the KSK wind direction appears more pronounced than at the westerly edge (dir$_{KSS}$–dir$_{KSK}$, Fig. 9).

For most wind directions, higher turbulent sensible heat fluxes are recorded at KSS (on average $Q_{H\,KSK}/Q_{H\,KSS} \approx 0.6$). However, a clear response to the flow characteristics discussed is evident (Fig. 9e). As noted (Section 4.3), channelling along the river and possible horizontal advection may influence the observations when wind is from the south (dir$_{KSS} \approx 185$–$205°$) and the southeast (dir$_{KSS} \approx 115$–$140°$). However, as this direction has been rarely observed at KSK and associated with low sensible heat fluxes at KSS (cf. Fig. 8), this results in values close to 1 (Fig. 9e). From the southeast (dir$_{KSS} \approx 90$–$145°$), sensible heat fluxes are smaller at KSS than at KSK. Any bluff body effect impacting the flow at KSK would play a role (dir$_{KSS} \approx 100$–$115°$), but higher wind speeds usually do not favour buoyancy. We speculate the higher Q_H at KSK may be induced by the nearby building facets. The sensible heat fluxes are more similar for the southerly directions (dir$_{KSS} \approx 185$–$205°$) so that the heat flux remains higher than that observed at the lower measurement level, with ratios around $Q_{H\,KSK}/Q_{H\,KSS} \approx 0.7$ (Fig. 9e). Sensible heat flux at KSK is about half that of KSS for westerly flow conditions, where surface drag and wind speed at the two heights were found to be very similar (dir$_{KSS} \approx 210$–$280°$). For northerly directions (dir$_{KSS} \approx 330$–$10°$), where wind speed (Fig. 9b) and friction velocity (Fig. 9c) indicate a systematic vertical wind profile, the sensible heat fluxes are nearly identical (also when comparing individual values, not shown). Here, the median ratio is close to unity.

Obviously, variations in anthropogenic heat sources and net storage heat flux relate to the urban canopy structure, and will impact the turbulent sensible heat fluxes observed. The canopy structure influences both the blending height, and the ability to transport heat, momentum, moisture and other constituents above the roughness sub layer. The latter is illustrated by the example of horizontal advection, induced by the channelling along the river. Such surface variations have been found to affect the flow in the surface layer elsewhere. For example, an inter-site comparison by Schmid et al. (1991) revealed that rather small surface variations can significantly impact the turbulent fluxes measured, even when the measurement height is likely above the roughness sublayer and the heterogeneity of the urban surface is classified as well-mixed at the local-scale. In their study, local-scale differences were of nearly comparable order of magnitude to urban–rural differences found elsewhere. Accordingly, the differences found between KSK and KSS could provide an estimate of the expected variations within the local-scale.

5. Implications for turbulent source area models and siting of EC systems

The results presented illustrate the challenges micrometeorological research faces in the complex, dense urban environments. Observations at the higher measurement level (KSS) were influenced by regional to local-scale advection, and local-scale roughness elements and bluff body effects of the urban surface. The micro-scale features were more evident in the measurements at the lower level (KSK) indicating it was within the roughness sublayer. The internal boundary layers that develop over the nearby river surface have likely not developed to sufficient height to reach the flux towers, so the latent heat fluxes remained small. The low vegetation cover, the complex arrangement of anthropogenic (heat and moisture) emissions and probably most importantly the immense variability of the three dimensional structure of the urban canopy (affecting radiation fluxes, heat storage flux, surface roughness and flow conditions) all make it difficult to interpret the observed quantities simply.

As is well known for surface energy balance measurements, in order to measure turbulent fluxes representative at the local-scale, a homogeneous fetch is considered a crucial requirement. Further, it is recommended to choose a sensor height well above the blending height. Measurements should be located far away from any object with bluff body characteristics, far away from chimneys and other micro-scale sources of anthropogenic emissions, and be sufficiently distant from large-scale surface changes that might induce horizontal advection. Obviously, every effort should be made by those using eddy covariance for local-scale turbulent exchanges to follow those guidelines. However, in cities, and especially their dense centres, it is often challenging to find these 'ideal', suitable locations, simply due to the heterogeneous nature of the urban canopy and/or due to logistical constraints (e.g. access etc.).

Still, the patchiness of surface form and materials are the reality of cities and hence of specific interest. In order to adequately capture such aspects, measurement strategies need to be designed carefully and properly adapted to the urban setting. Where ideal measurement locations cannot be chosen, it may be advisable to operate a series of sites in proximity. As the current study shows, a second tower, even with a lower sensor height within the roughness sublayer, has the potential to add useful information for the interpretation of fluxes measured. And, as indicated with respect to radiative source areas (Section 2.3.2), multiple measurements would improve the spatial representativeness. In addition to profile measurements (EC observations at different height/horizontal distances) other measurement approaches (such as surface or atmospheric remote sensing) obviously can add useful information for the interpretation of the fluxes measured.

Data need to be analysed in combination with adequate footprint models that can treat the complex urban areas appropriately. The site described in this study illustrates some of the more sophisticated requirements that need to be incorporated into future footprint models. Where surface heterogeneities are low, it is probably acceptable to rely on simple wind direction sector analysis. However, over patchy surfaces, such as those including larger parks or river surfaces, the application of simple models provides only very first order results as likely internal boundary layers and advective fluxes are not accounted for. Such features will need to be addressed by footprint models aiming to be applicable to the real urban surface. However, such models need to be computationally efficient and address the range of atmospheric stability, most notably urban areas' unstable conditions.

6. Conclusions

Urban climate observations are often constrained by logistics (e.g. safety, planning, economic, operations, maintenance, access etc.). This results in few sensors being installed and typically only in restricted locations. Modelling of surface atmosphere exchanges are also challenged by urban environments, especially in complex central business districts (CBD). Nevertheless, it is critical to understand the atmospheric processes within these areas, given this is where many people live and work. The analysis of fluxes observed at two nearby sites in central London allows some conclusions to be drawn about urban surface energy exchanges. Moreover, it demonstrates methodological challenges of research in CBD that have clear implications for future studies.

Radiation measurements are impacted by the anisotropic nature of the urban surface and the high reflectance materials increasingly being used in buildings. With sufficient irradiance, the surface albedo is influenced by strong specular reflections or reflection glare. The surface deviates distinctly from Lambertian characteristics. This highlights the need to consider the source area of radiometers in terms of both diffuse and direct irradiance. Accounting for reflections of direct irradiance, which depend on the solar position relative to the site (i.e. latitude, time), sensor height, and the BRDF of the observed surface (described by a combination of conditions at various scales from material properties to three-dimensional canopy structure) allows apparently anomalous reflected short-wave radiation to be explained.

Spatial patterns of surface albedo suggest that the lower bulk surface albedo observed at the site with the greater measurement height ($\overline{\alpha} = 0.11$ at KSS) better represents the local-scale area, whereas instruments located at a lower elevation show a bias towards roof surfaces ($\overline{\alpha} = 0.14$ at KSK). Under overcast conditions at both sites, the bulk surface albedo is close to these median albedo values (higher by 0.01). Using cloud cover information, it is shown that the impact of specular reflections on surface albedo measurements is highly accentuated under clear sky conditions and decreases with increasing cloud cover. In London, above 70% cloud cover diffuse radiation mostly dominates over the direct flux.

An analytical footprint model was used to relate the observed turbulent fluxes of sensible and latent heat to surface controls from different land cover types. Land cover fractions derived from this modelled turbulent flux source area indicated that high turbulent sensible heat fluxes occur where impervious surface fractions are particularly high. However, the modelled source area characteristics did not fully explain the spatial variations of the turbulent fluxes. Sensible heat flux was lower from directions potentially affected by a nearby open water surface, the River Thames. However, this did

not seem to be related to the moisture supplied and its potential impact on the partitioning of available energy, as there is no clear increase in turbulent latent heat fluxes. Rather, the river has a decrease in surface roughness, so the decrease in sensible heat fluxes was explained by channelling of the flow and potential horizontal advection. The impact of the river on the observed fluxes might have been further limited if the internal boundary layers that form over the water surface do not develop to the height of the flux towers. Such effects are not captured by the analytical footprint model. Probably, detailed LES modelling could provide some insights.

It has not been possible to quantify precisely the role of vegetation as a moisture source for the latent heat fluxes, given its generally small surface coverage. While no clear signal was found in the latent heat flux corresponding to the nearby water surface (presumably due to the formation of internal boundary layers) or the sparse vegetation, rainfall appeared to be a key driving-factor for evaporation in this dense urban environment. When the urban fabric was wet, mostly associated with south-westerly flow (i.e. frontal systems connected to mid-latitude cyclones), the generally small latent heat flux magnitude did increase. However, the response to rainfall could not be isolated from the influence of the vegetated areas and their soil moisture content.

While only limited conclusions could be drawn from the source area analysis, because of the spatial distribution of the land cover types (e.g. no area with particularly high vegetation in the flux footprint) and the applicability of the model under such complex conditions (e.g. three dimensional building form, advection along the river), the analysis of flow patterns proved more suitable. Comparison of the two measurement heights suggested the spatial variations of the sensible heat flux observed were related to changes in surface roughness. Measurements at the higher level clearly picked up the larger scale channelling induced by the riverbed, while bluff body effects explained variations at the lower level. Where the source areas were most homogeneous (areas with greatest built density), flow conditions were vertically consistent. The wind velocity profile was similar to the log-law and sensible heat flux appeared to be invariant with height, even if initial morphometric parameters suggested the measurements may be below the blending height. These findings indicate that the investigation of turbulence statistics may be more informative in the interpretation of turbulent fluxes than detailed calculations of surface cover fractions without detailed 3D information incorporated. Also, it highlights that parameterisations of morphometric characteristics need to be further evaluated for such complex settings.

This work demonstrates, even in this complex setting, observations provide useful information about processes governing surface-atmosphere exchange that must be understood in the context of global urbanisation and climate change adaptation strategies. Detailed analysis and careful interpretation do allow us to describe and move towards quantifying atmospheric conditions in the CBD. This study identified limitations to some current observational approaches, including critical aspects of instrument siting in complex urban settings and where more detailed, better adapted footprint models are required. All fluxes of the surface energy balance are highly scale dependant, which needs to be considered when interpreting measured (as well as modelled) energy fluxes in relation to each other. Both for radiometer and EC flux measurements, it is suggested that simultaneous operation of two nearby sites can greatly benefit the analysis. Multiple radiation sensors could be combined to be more representative of the turbulent flux footprint. The results provide an example of how observations within the roughness sublayer can be interpreted, also with respect to the impact of bluff bodies. Clearly more measurements are needed from such settings, but this work underlines the requirement for careful directional analysis and interpretation of such datasets.

Measurement and modelling approaches may be pushed to their limits in dense urban settings, but if urban climate research is to contribute to the challenges of real cities those limits have to be addressed. To manage cities sustainably and smartly, currently and into the future under changing climates, measurements and models must also consider central urban areas where interactions of humans with the environment are particularly concentrated. Surface heterogeneities that have proven to challenge both measurements and modelling techniques in this study are at the scale where urban planning strategies are implemented (e.g. usage of high reflectance materials, orientation of buildings, etc.). Measurements will allow improved understanding of the processes, enhanced modelling skill and better forecasting with data assimilation to help make cities more resilient.

Acknowledgements

References

Aubinet, M., Heinesch, B., Yernaux, M., 2003. Horizontal and vertical Co2 advection in a sloping forest. Bound.-Layer Meteorol. 108, 397–417.

Aubinet, M., Feigenwinter, C., Heinesch, B., Bernhofer, C., Canepa, E., Lindroth, A., Montagnani, L., Rebmann, C., Sedlak, P., Van Gorsel, E., 2010. Direct advection measurements do not help to solve the night-time CO2 closure problem: evidence from three different forests. Agric. For. Meteorol. 150, 655–664.

Bohnenstengel, S.I., Evans, S., Clark, P.A., Belcher, S.E., 2011. Simulations of the London urban heat island. Quart. J. R. Meteorol. Soc. 137, 1625–1640.

Chemel, C., Sokhi, R.S., 2012. Response of London's urban heat island to a marine air intrusion in an easterly wind regime. Boundary Layer Meteorol. 144, 65–81.

Christen, A., 2005. Atmospheric turbulence and surface energy exchange in urban environments. University of Basel, 142 pp..

Christen, A., Vogt, R., 2004. Energy and radiation balance of a Central European City. Int. J. Climatol. 24, 1395–1421.

Christen, A., Coops, N.C., Crawford, B.R., Kellett, R., Liss, K.N., Olchovski, I., Tooke, T.R., van der Laan, M., Voogt, J.A., 2011. Validation of modeled carbon-dioxide emissions from an urban neighborhood with direct eddy-covariance measurements. Atmos. Environ. 45, 6057–6069.

Coutts, A.M., Beringer, J., Tapper, N.J., 2007. Impact of increasing urban density on local climate: spatial and temporal variations in the surface energy balance in Melbourne, Aust.. J. Appl. Meteorol. Clim. 46, 477–493.

Crawford, B., Grimmond, C.S.B., Christen, A., 2011. Five years of carbon dioxide fluxes measurements in a highly vegetated suburban area. Atmos. Environ. 45, 896–905.

Elliott, W.P., 1958. The growth of the atmospheric internal boundary layer. Trans. Am. Geophys. Union 39, 1048.

Feigenwinter, C., Bernhofer, C., Eichelmann, U., Heinesch, B., Hertel, M., Janous, D., Kolle, O., Lagergren, F., Lindroth, A., Minerbi, S., Moderow, U., Mölder, M., Montagnani, L., Queck, R., Rebmann, C., Vestin, P., Yernaux, M., Zeri, M., Ziegler, W., Aubinet, M., 2008. Comparison of horizontal and vertical advective CO_2 fluxes at three forest sites. Agric. For. Meteorol. 148, 12–24.

Feigenwinter, C., Vogt, R., Christen, A., 2012. Eddy covariance measurements over urban areas. In: Aubinet, M., Vesala, T., Papale, D. (Eds.), Eddy Covariance: A Practical Guide to Measurement and Data Analysis. Springer Atmospheric Sciences, pp. 377–397.

Fortuniak, K., Pawlak, W., Siedlecki, M., 2012. Integral turbulence statistics over a Central European City centre. Bound.-Layer Meteorol. 146, 257–276.

Frey, C.M., Parlow, E., 2012. Flux measurements in Cairo. Part 2: On the determination of the spatial radiation and energy balance using ASTER satellite data. Remote Sens. 4, 2635–2660.

Gash, J.H.C., 1986. A note on estimating the effect of a limited fetch on micrometeorological evaporation measurements. Bound.-Layer Meteorol. 35, 409–413.

Gioli, B., Toscano, P., Lugato, E., Matese, A., Miglietta, F., Zaldei, A., Vaccari, F.P., 2012. Methane and carbon dioxide fluxes and source partitioning in urban areas: the case study of Florence, Italy. Environ. Pollut. 164, 125–131.

Göckede, M., Markkanen, T., Hasager, C.B., Foken, T., 2006. Update of a footprint-based approach for the characterisation of complex measurement sites. Bound.-Layer Meteorol. 118, 635–655.

Grimmond, C.S.B., Salmond, J.A., Oke, T.R., Offerle, B., Lemonsu, A., 2004. Flux and turbulence measurements at a dense urban site in Marseille: heat, mass (water, carbon dioxide) and momentum. J. Geophys. Res. Atmos. 109, 19.

Hiller, R., McFadden, J., Kljun, N., 2011. Interpreting CO_2 fluxes over a suburban lawn: the influence of traffic emissions. Bound.-Layer Meteorol. 138, 215–230.

Horst, T.W., Weil, J.C., 1992. Footprint estimation for scalar flux measurements in the atmospheric surface layer. Bound.-Layer Meteorol. 59, 279–296.

Hsieh, C., Katul, G., Chi, T., 2000. An approximate analytical model for footprint estimation of scalar fluxes in thermally stratified atmospheric flows. Adv. Water Resour. 23, 765–772.

Iamarino, M., Beevers, S., Grimmond, C.S.B., 2012. High-resolution (space, time) anthropogenic heat emissions: London 1970–2025. Int. J. Climatol. 32, 1754–1767.

Iwata, T., Kimura, K.-I., Shukuya, M., Takano, K., 1991. Discomfort caused by wide-source glare. Energ. Build. 15, 391–398.

Järvi, J., Hannuniemi, H., Hussein, T., Junninen, H., Aalto, P.P., Hillamo, R., Mäkelä, T., Keronen, P., Siivola, E., Vesala, T., Kulmala, M., 2009. The urban measurement station SMEAR III: continuous monitoring of air pollution and surface-atmosphere interactions in Helsinki, Finland. Boreal Environ. Res. 14 (Suppl. i), 86–109.

Kanda, M., Moriwaki, R., Kasamatsu, F., 2006. Spatial variability of both turbulent fluxes and temperature profiles in an urban roughness layer. Bound.-Layer Meteorol. 121, 339–350.

Kljun, N., Rotach, M.W., Schmid, H.P., 2002. A three-dimensional backward Lagrangian footprint model for a wide range of boundary-layer stratifications. Bound.-Layer Meteorol. 103, 205–226.

Kljun, N., Calanca, P., Rotach, M.W., Schmid, H.P., 2004. A simple parameterisation for flux footprint predictions. Bound.-Layer Meteorol. 112, 503–523.

Kordowski, K., Kuttler, W., 2010. Carbon dioxide fluxes over an urban park area. Atmos. Environ. 44, 2722–2730.

Kormann, R., Meixner, F.X., 2001. An analytical footprint model for non-neutral stratification. Bound.-Layer Meteorol. 99, 207–224.

Kotthaus, S., Grimmond, C.S.B., 2012. Identification of micro-scale anthropogenic CO_2, heat and moisture sources – processing eddy covariance fluxes for a dense urban environment. Atmos. Environ. 57, 301–316.

Kotthaus, S., Grimmond, C.S.B., 2013. Energy exchange in a dense urban environment – Part I: Temporal variability of long-term observations in central London. Urban Climate 10 (P2), 261–280.

Lemonsu, A., Grimmond, C.S.B., Masson, V., 2004. Modeling the surface energy balance of the core of the Old Mediterranean City: Marseille. J. Appl. Meteorol. 43, 312–327.

Lindberg, F., Grimmond, C.S.B., 2010. Continuous sky view factor from high resolution urban digital elevation models. Clim. Res. 42 (3), 177–183.

Lindberg, F., Grimmond, C.S.B., 2011. The influence of vegetation and building morphology on shadow patterns and mean radient temperatures in urban areas: model development and evaluation. Urb. Ecosys. 105, 311–323.

Liu, H.Z., Feng, J.W., Järvi, L., Vesala, T., 2012. Four-year (2006–2009) eddy covariance measurements of CO2 flux over an urban area in Beijing. Atmos. Chem. Phys. 12, 7881–7892.

Loridan, T., Grimmond, C.S.B., 2012. Characterization of energy flux partitioning in urban environments: links with surface seasonal properties. J. Appl. Meteorol. Climatol. 51, 219–241.

Lucht, W., Schaaf, C.B., Strahler, A.H., 2000. An algorithm for the retrieval of albedo from space using semiempirical BRDF models. IEEE Trans. Geosci. Remote 38, 977–998.

Macdonald, R.W., Griffiths, R.F., Hall, D.J., 1998. An improved method for the estimation of surface roughness of obstacle arrays. Atmos. Environ. 32, 1857–1864.

Mårtensson, E.M., Nilsson, E.D., Buzorius, G., Johansson, C., 2006. Eddy covariance measurements and parameterisation of traffic related particle emissions in an urban environment. Atmos. Chem. Phys. 6, 769–785.

Met Office, 2012a. Met Office Integrated Data Archive System (MIDAS) Land and Marine Surface Stations Data (1853-current). NCAS British Atmospheric Data Centre. URL http://badc.nerc.ac.uk/browse/badc/ukmo-midas (accessed 7.16.13).

Met Office, 2012b. Regional Climates: Southern England. URL http://www.metoffice.gov.uk/climate/uk/so/ (accessed 3.5.13).

Mulhearn, P.J., Finnigan, J.J., 1978. Turbulent flow over a very rough, random surface. Boundary Layer Meteorol. 15, 109–132.

Nordbo, A., Järvi, L., Haapanala, S., Moilanen, J., Vesala, T., 2012. Intra-city variation in urban morphology and turbulence structure in Helsinki, Finland. Bound.-Layer Meteorol. 146, 469–496.

Offerle, B., Grimmond, C.S.B., Oke, T.R., 2003. Parameterization of net all-wave radiation for urban areas. J. Appl. Meteorol. 42, 1157–1173.

Offerle, B., Grimmond, C.S.B., Fortuniak, K., Pawlak, W., 2006. Intraurban differences of surface energy fluxes in a Central European City. J. Appl. Meteorol. 45, 125–136.

Oke, T.R., 1987. Boundary Layer Climates, 2nd ed. London and John Wiley & Sons, New York, Co-published by Routledge, p. 435.

Park, C., Schade, G.W., Boedeker, I., 2011. Characteristics of the flux of isoprene and its oxidation products in an urban area. J. Geophys. Res. 116, D21303.

Pauscher, L., 2010. Scintillometer Measurements above the Urban Area of London. Universität Bayreuth, p. 95.

Pawlak, W., Fortuniak, K., Siedlecki, M., 2011. Carbon dioxide flux in the centre of Lodz, Poland – analysis of a 2-year eddy covariance measurement data set. Int. J. Climatol. 31, 232–243.

Pigeon, G., Lemonsu, A., Grimmond, C.S.B., Durand, P., Thouron, O., Masson, V., 2007. Divergence of turbulent fluxes in the surface layer: case of a Coastal City. Bound.-Layer Meteorol. 124, 269–290.

Rannik, Ü., Sogachev, A., Foken, T., Göckede, M., Kljun, N., Leclerc, M.Y., Vesala, T., 2012. Footprint analysis. In: Aubinet, M.A. (Ed.), Eddy Covariance: A Practical Guide to Measurement and Data Analysis. Springer Atmospheric Sciences, pp. 212–261.

Raupach, M.R., Shaw, R.H., 1982. Averaging procedures for flow within vegetation canopies. Bound.-Layer Meteorol. 22, 79–90.

Raupach, M.R., Thom, A.S., Edwards, I., 1980. A wind-tunnel study of turbulent flow close to regularly arrayed rough surfaces. Bound.-Layer Meteorol. 18, 373–397.

Roberts, S.M., 2010. Three-dimensional radiation flux source areas in urban areas. University of British Columbia, p. 214.

Rotach, M., 1995. Profiles of turbulence statistics in and above an urban street canyon. Atmos. Environ. 29 (13), 1473–1486.

Rotach, M.W., Vogt, R., Bernhofer, C., Batchvarova, E., Christen, A., Clappier, A., Feddersen, B., Gryning, S.-E., Martucci, G., Mayer, H., Mitev, V., Oke, T.R., Parlow, E., Richner, H., Roth, M., Roulet, Y.-A., Ruffieux, D., Salmond, J.A., Schatzmann, M., Voogt, J.A., 2005. BUBBLE – an urban boundary layer meteorology project. Theor. Appl. Climatol. 81, 231–261.

Salmond, J.A., Roth, M., Oke, T.R., Christen, A., Voogt, J.A., 2012. Can surface-cover tiles be summed to give neighborhood fluxes in cities? J. Appl. Meteorol. Clim. 51, 133–149.

Schmid, H.P., 1994. Source areas for scalars and scalar fluxes. Bound.-Layer Meteorol. 67, 293–318.

Schmid, H.P., 1997. Experimental design for flux measurements: matching scales of observations and fluxes. Agric. For. Meteorol. 87, 179–200.

Schmid, H.P., Lloyd, C.R., 1999. Spatial representativeness and the location bias of flux footprints over inhomogeneous areas. Agric. For. Meteorol. 93, 195–209.

Schmid, H.P., Cleugh, H.A., Grimmond, C.S.B., Oke, T.R., 1991. Spatial variability of energy fluxes in suburban terrain. Bound.-Layer Meteorol. 54, 249–276.

Schuepp, P.H., Leclerc, M.Y., MacPherson, J.I., Desjardins, R.L., 1990. Footprint prediction of scalar fluxes from analytical solutions of the diffusion equation. Bound.-Layer Meteorol. 50, 355–373.

Shih, N.-J., Huang, Y.-S., 2001. An analysis and simulation of curtain wall reflection glare. Build. Environ. 36, 619–626.

Sogachev, A., 2009. A note on two-equation closure modelling of canopy flow. Bound.-Layer Meteorol. 130, 423–435.

Sogachev, A., Lloyd, J., 2004. Using a one-and-a-half order closure model of the atmospheric boundary layer for surface flux footprint estimation. Bound.-Layer Meteorol. 112, 467–502.

Soux, A., Voogt, J.A., Oke, T.R., 2004. A model to calculate what a remote sensor 'sees' of an urban surface. Bound.-Layer Meteorol. 111, 109–132.

Stewart, I.D., Oke, T.R., 2012. "Local Climate Zones" for urban temperature studies. Bull. Am. Meteorol. Soc. 93, 1879–1900.

Van de Boer, A., Moene, A.F., Schüttemeyer, D., Graf, A., 2013. Sensitivity and uncertainty of analytical footprint models according to a combined natural tracer and ensemble approach. Agric. Forest. Meteorol. 169, 1–11.

Vesala, T., Jarvi, L., Iauniainen, S., Sogachev, A., Rannik, U., Mammarella, I., Siivola, E., Keronen, P., Rinne, J., Riikonen, A., Nikinmaa, E., 2008a. Surface-atmosphere interactions over complex urban terrain in Helsinki, Finland. Tellus 60B, 188–199.

Vesala, T., Kljun, N., Rannik, U., Rinne, J., Sogachev, A., Markkanen, T., Sabelfeld, K., Foken, T., Leclerc, M.Y., 2008b. Flux and concentration footprint modelling: state of the art. Environ. Pollut. 152, 653–666.

Vesala, T., Kljun, N., Rannik, Ü., Sogachev, A., Markkanen, T., Sabelfeld, K., Foken, T., Leclerc, M.Y., 2010. Flux and concentration footprint modelling. In: Hanrahan, G. (Ed.), Modelling of Pollutants in Complex Environmental Systems. ILM Publications, St Albans, pp. 339–355.

Weber, S., Kordowski, K., 2010. Comparison of atmospheric turbulence characteristics and turbulent fluxes from two urban sites in Essen, Germany. Theor. Appl. Climatol. 102, 61–74.

Wood, C.R., Pauscher, L., Ward, H.C., Kotthaus, S., Barlow, J.F., Gouvea, M., Lane, S.E., Grimmond, C.S.B., 2013. Wind observations above an urban river using a new lidar technique, scintillometry and anemometry. Sci. Total Environ. 442, 527–533.

Yang, X., 2011. Urban Remote Sensing: Monitoring, Synthesis and Modeling in the Urban Environment. Wiley-Blackwell, Chichester, UK, 388 pp.